5. Carboxymethyl chitosan capped bimetallic nanoparticles entrapped in theranostic nanofibers

Nanoparticles prepared using CMC, a versatile derivative of chitosan, retains and even enhances the antimicrobial properties of its parent compound while offering improved solubility and biocompatibility. CMC exhibit antimicrobial properties through various mechanisms like disruption of microbial cell membranes, metal ion release, formation of physical barrier and generation of reactive oxygen species. To enhance the long-term antimicrobial efficacy of nanoparticles, embedding them in porous matrix-based nanofibers often recommended, as this configuration facilitates a controlled release and sustained delivery of the therapeutic compound derived from the extracellular matrix to the site of infection by MDR bacteria. Nanocomposites consisting of nanofibers loaded metallic nanoparticles have garnered significant interest as a viable resolution to this issue. Therefore, nanofibers are regarded as a very promising system for wound dressing, due to their capability for broad applicability of major injuries and infections. In recent times, there has been a surge in the popularity of nanofiber dressings made up of nanoparticles. This is because they possess the capability to meet the complex requirements of the biophysiological surroundings at the location of a microbial infection, which regular wound care materials are incapable of fulfilling.

The human cationic antimicrobial polypeptide LL-37, the chief component of the cathelicidin family identified in humans thus far, plays a critical function within the innate-immune defense, serving as a primary defense mechanism against a wide range of invading pathogens. Extensive research on LL-37 has demonstrated that it exhibits direct bactericidal activity against numerous pathogens, including *P. aeruginosa* and *S. aureus,* along with others. Concerning *P. aeruginosa*, LL-37 is instrumental in inhibiting biofilm formation at low concentrations and even disrupts the established biofilms at higher dosages. Biofilms

represent a major challenge in the application of antibiotics for treating chronic infections. The primary challenge linked to LL-37 administration is its rapid degradation; hence, substantial dosages or gene therapy are necessary to achieve therapeutic benefits. Consequently, the development of effective LL-37-based approaches integrated with nanotechnology is crucial for enhancing the half-life of LL-37 that aid in tackling multidrug-resistant bacterial infections effectively in wound management.

Magnesium (Mg), an alkaline earth metal, is inherently present in substantial quantities within the human body, where it serves as a vital metabolite and catalytic agent in numerous metabolic pathways. In its Mg^{2+} ionic form, it is efficiently absorbed without inducing cytotoxicity or excessive accumulation. Owing to these intrinsic biological properties, metallic magnesium holds significant potential for the synthesis of fluorescent nanoclusters with enhanced applicability in *in vivo* biomedical research. This study explores the utilization of ultra-small magnesium nanoclusters (USM) as imaging agents for the fabrication of theranostic nanoparticles, capitalizing on their remarkable biocompatibility, biodegradability, and non-toxic profile. Their unique physicochemical properties—particularly high surface reactivity, biocompatibility, and the potential for biodegradable applications—position them as an emerging alternative in the field of nanomedicine. While gold–silver systems provide stability and antimicrobial efficacy, magnesium nanoclusters introduce the additional advantage of being earth-abundant, cost-effective, and less likely to accumulate in biological tissues. Presenting these materials alongside noble metal nanoparticles therefore broadens the scope of the thesis and emphasizes the need to evaluate diverse classes of nanostructures for safe and sustainable biomedical applications. Here, USM has been only employed to assess the nanoparticles' retention time and biodistribution within biological systems.

In this study, we have developed a useful strategy for treating MDR microbial infection by preparing wound dressing nanofibers composed of CMC coated gold-silver-LL-37 nanoparticles (G-S-CMC-Pep-NPs-NFs). Addressing resistant microbial wounds while mitigating adverse reactions has consistently presented a significant challenge. For this, we, for the very first time, have engineered G-S-CMC-Pep-NPs-NFs for *in vivo* applications of wound. Preliminarily prepared G-S-CMC-Pep-NPs-NFs were examined for its size, polydispersity index, surface charge, and topology of surface. Further, Significantly, G-S-CMC-Pep-NPs-NFs anti-microbial efficacy was assessed against MDR microbes of *P. aeruginosa* and *S. aureus* through *in vitro* investigations in relation to a commercially available broad-range antimicrobial agent. G-S-CMC-Pep-NPs were homogeneously distributed within nanofibers matrix utilizing the electrospinning technique. The nanofibers were subsequently employed to wound sites in mice infected with MDR microbes. Their wound healing efficacy was evaluated through multiple parameters, including wound closure rates, re-epithelialization, the expression levels of wound-related proteins, and assessment via ultrasound and photoacoustic imaging techniques. Additionally, the molecular mechanism underlying the enhancement of wound healing was elucidated through the analysis of protein expression levels associated with specific signaling pathways. Also, real-time wound visualization, along with assessments of angiogenesis, vascularization, and wound oxygen saturation levels, were conducted for comprehensive evaluation. A schematic representation of the objective, specific aims and postulated hypothesis of the present work is shown in **Figure 5.1.**

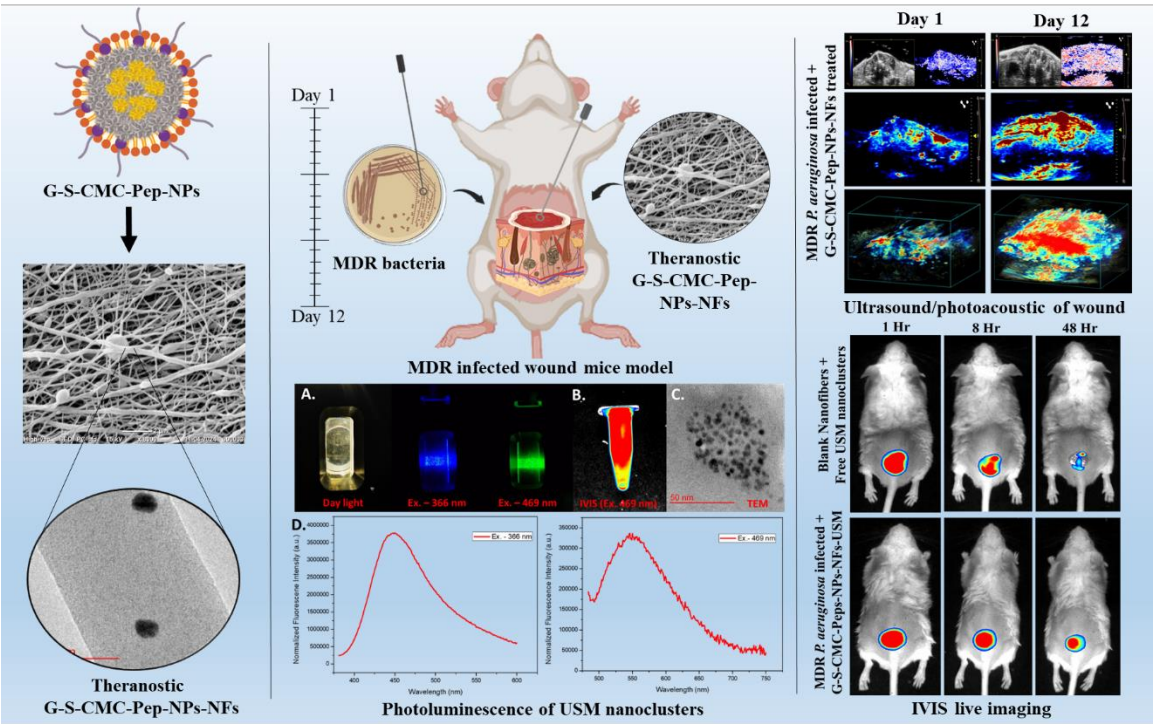

Figure 5.1. Schematic representation of objectives and hypothesis

5.1. Materials

Carboxymethyl-chitosan, (deacetylation degree~90%) was procured from GLR innovations New Delhi, India. Gold-III chloride-trihydrate ($HAuCl_4 \cdot 3H_2O$) and silver nitrate ($AgNO_3$), polyvinyl alcohol $(C_2H_4O)n$, tween-80, and chitosan (MW ~ 30kDa, deacetylation degree ≥90%) were bought from SRL Pvt. Ltd. India. LL-37 peptide was purchased from GCC Biotech (India) Pvt. Ltd. Magnesium chloride and bovine serum albumin were supplied by Merck India. Microbiological media such as Muller Hinton agar and Muller Hinton broth were bought from Hi-Media Lab Pvt. Ltd., India. LIVE-DEAD Bac-Light Bacterial Kit for Viability (L7-012) was bought from Molecular Probes, Invitrogen (Grand Island, New York, USA). β-Actin (13-E5) Rabbit mAb (45kDa), Vimentin (D21-H3) XP-Rabbit mAb (57kDa), Phospho-p44-42-MAPK, Erk-1/2 (Thr-202/Tyr-204) (D13144E), Rabbit-XP monoclonal antibody (44, 42kDa) procured from CST (CST, Beverly, Massachusetts). TGF-beta1 (44kDa) was bought from Elabscience

Biotechnology (Texas, USA). Reagents employed in the experiments were of an analytically pure quality.

5.2. Methods

5.2.1. Fabrication and characterization of G-S-CMC-Pep-NPs

Fabrication of gold-silver nucleus-shell formulation was achieved by a seeded growth methodology, where gold nanoparticles were used as the seed compound. Succinctly, 1.5 ml of pre-synthesized gold nanoparticles preparation was added to 8.5 ml of deionized or distilled water at a temperature of 85°C for two hours. Following, $HAuCl_4 \cdot 3H_2O$ and $AgNO_3$ were combined in various molar ratios (1:0.25, 1:0.5, 1:0.75 1:1, 1:2, and 1:3), together with a 2 % solution of CMC measuring 10 ml **(Table 5.1.)**. Subsequently, the concoction was stirred on a magnetic stirrer and temperature was maintained at 85°C. The CMC solution served for two purposes; reductive factor and a capping compound. The solution exhibits a chromatic transition from pink to a profound purple to light brown hue within a duration of 15-20 min, resulting in the synthesis of G-S formulation. Additionally, duration of two hours was designated for the completion of the reaction. Afterwards, CMC is cross-linked with the inclusion of a re-suspending agent (Tween80) to prevent the occurrence of particle clusters during the purifying process. For this, a 5 ml solution of CMC in distilled water was made at a concentration of 10 mg/ml and containing 1 percent (w/v) Tween-80. With constant stirring at 37°C and a pH of 6, a sodium tri-polyphosphate (TPP) solution 1.5 mg/mL concentration was gradually added to the CMC solution, so that it finally turned to light orange which confirmed the generation of G-S-CMC-NPs. Furthermore, the LL-37 peptide was conjugated with the prepared G-S-CMC-NPs by electrostatic interaction mechanism. Here LL-37 is positively charged and CMC has carboxyl groups (-COOH) that can be deprotonated to form negatively charged carboxylate ions and there can be an electrostatic attraction between the LL-37 and the G-S-CMC-NPs.

To facilitate this, BSA and synthetic LL-37 were introduced into a 24-well plate at a 3:1 ratio and subsequently incubated in a temperature-controlled shaker at 37°C and 550 rpm for 3.5 hours to synthesize G-S-CMC-Pep-NPs. The solutions were filtered and then washed three times with deionized water to ensure complete removal of residual components. In the end, this process brought the pH down to around 7. To comparatively evaluate the antimicrobial efficacy of prepared G-S-CMC-Pep-NPs, four other formulations were also prepared additionally: gold nanoformulation (G-NPs), silver nanoformulation (S-NPs), and gold-silver nanoformulation (G-S-NPs), CMC-based silver nanoformulation (G-S-CMC-NPs).

Table 5.1. Formulation of various batches of nanoparticles

Batches	$AgNO_3$ 10mM (ml)	$HAuCl_4$ 10mM (ml)	Gold Seed (ml)	Ascorbic Acid 50mM (ml)	CMC 0.1% (ml)	CMC 2mg/ml (ml)	Na-TPP 1mg/ml (ml)	Tween 80 1%w/v (ml)	LL-37 (50 µg/ml) (Pep) (ml)
G-NPs	-	1	-	0.8	-	-	-	-	-
S-NPs	2	-	-	1	-	-	-	-	-
G-S-NPs	3	1	1	1.5	-	-	-	-	-
G-S-CMC-NPs	3	1	1	-	15	10	3	2.5	-
G-S-CMC-Pep-NPs	3	1	1	-	15	10	3	2.5	2.5

5.2.1.1. Size of particle, PDI, and zeta potential

Optimized nanoparticles were assessed for their particle size, and polydispersity index by dynamic light scattering technique using Malvern Zeta-sizer of Nanoseries. The charge on surface was determined using the electrophoretic light scattering technique.

5.2.1.2. Transmission electron microscopy analysis

TEM investigation, especially employing the Tecnai G2 20 TWIN equipment, was performed to evaluate the size, shape, and structure of the optimized formulations at the nanoscale. The drop casting procedure was use for sample preparation. The concentrated formulations were diluted in distilled water and afterward exposed to sonication for a period of 5 minutes. Samples were then dropped onto a copper grid of TEM comprised of copper covered with a carbon layer (size of mesh ~400). The droplets were allowed to evaporate out for a prolonged amount of time before undergoing analysis.

5.2.1.3. Atomic force microscopy analysis

The analysis of the optimized formulations' surface topology, size and shape were done with AFM by NT-MDT Service and Logistics Pvt. Ltd. The samples were diluted with milli-Q water during the preparation procedure. After sonication for 5 minutes, small drops of prepared formulation were put onto a microscopic slide (1×1cm) and then allowed for evaporation for 24 hours. The NOVA program, designed by NT-MDT platform was employed for imaging analysis to generate 2D and 3D-AFM images of the nanoformulations.

5.2.1.4. Energy dispersive spectroscopy analysis

The G-S-CMC-Pep-NPs were subjected to investigation including mapping and spectrum using EDS to identify and quantify elements in the nanoformulation to understand the formation of gold and silver in core.

5.2.2. Antimicrobial efficacy

5.2.2.1. Isolation of MDR microbes

MDR strains of Gram-ve microbes *P. aeruginosa* and Gram+ve microbes *S. aureus* were isolated from Sir Sunderlal Hospital, Varanasi, UP, India **(Figure 5.2.)**. Total thirty-three environmental wastewater samples were collected from five different sites- Down-stream

water (site 1); Intensive Care Unit (site 2); Pathology laboratory (site 3); Surgical ward (site 4); Water cooler sink (site 5). The samples were transferred to the laboratory under controlled temperature settings and were processed within a two-hour timeframe after collection. An aliquot of waste water from each sample underwent filtration using a 0.22 µm membrane filter. The filter membranes were then put on plate-count agar and aerobically incubated at 37°C for 24 to 48 hr. Followed by incubation, *P. aeruginosa* and *S. aureus* colonies were selected and transferred to their selective agars based on their colony form. The isolated organisms were then identified biochemically using conventional procedures after producing pure colonies.

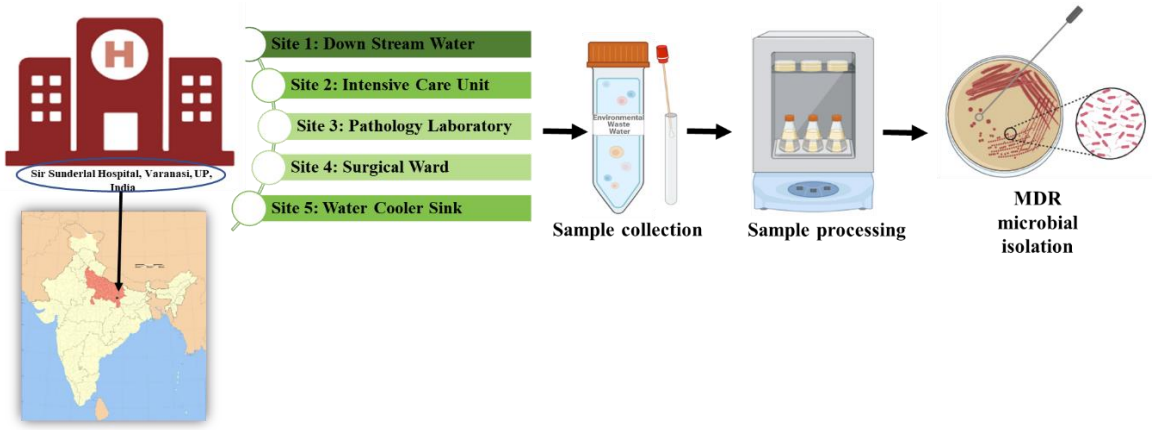

Figure 5.2. Graphical illustration of isolation of microbes from different environmental wastes

5.2.2.2. Antimicrobial susceptibility testing

Antimicrobial susceptibility analysis was conducted using Mueller-Hinton medium against amoxicillin (10µg), doxycycline (15 µg), clarithromycin (5µg), cefuroxime (10µg), metronidazole (5µg), cephalixin (20µg), ciprofloxacin (5µg), sulfamethoxazole (5µg) and chloramphenicol (30µg). The plates were then incubated under aerobic conditions at 37°C for 18 to 24 hr. Inhibition zones were measured and evaluated in accordance with the guidelines established by the National Committee for Clinical Laboratory Standards [161].

5.2.2.3. Estimation of minimum inhibitory concentration and minimum bactericidal concentration

This study aimed to assess the minimum concentration of the nanoformulations necessary to completely eliminate the viability of the initial microbial inoculate. The optimized formulations were evaluated to determine the minimum inhibitory concentration (MIC) and minimum bactericidal concentration (MBC) against Gram +ve and Gram -ve strains, each with a microbial load of 10^7–10^8 CFU/ml, using 96 wells culture plate. The bacterial strains were subjected to a liquid broth that included variable concentrations of optimised nanoformulations, ranging from 200 μg/ml to 0.097 μg/ml. This was accomplished by a two-fold serial dilution technique. The MIC values were assessed by identifying the lowest concentration of the nanoparticles that effectively inhibited bacterial cell growth. To investigate the impact of near-MIC treatment on bacterial growth, optical density (OD) measurements were performed by bacterial growth curve. This investigation aimed to assess the minimal concentration of the nanoformulations necessary to completely eliminate the viability/ visibility of the initial bacterial inoculate.

5.2.2.4. Disc diffusion method

Disc diffusion method was performed to examine the antibacterial sensitivity of the nanoformulations countering both microbiological grams' strain. Mueller Hinton nutrient medium were being prepared by distributing the Mueller Hinton Broth in microbiological cultured medium. The sterilized grade 1 Whatman paper of 5 mm in diameter was soaked with nanoformulations and a commercially available Ciprofloxacin antibiotic. The discs were subsequently put onto the outer surface of different Mueller-Hinton agar plates which contains strains of both the MDR microbes using sterile forceps. The plates were then incubated overnight at 37°C. Zone of inhibition (ZOI) was recorded in mm (diameter) by

utilizing ordinary scale for measuring. This was conducted to assess the resistant rate and comparative efficacy of all improved formulations in relation to the conventional medicine.

5.2.2.5. Antibiofilm assay

To assess the antibiofilm effectiveness of optimized formulations against various strains of microbes, glass slides with interface surface area of 1.3 cm^2 were employed as substrates for biofilm deposition through the drop-casting technique. The dispersion was allowed to dry for 24 hr at 37°C, followed by drying at 70°C for an extra hour. The untreated bacterial biofilm served as the experimental control for comparison. The morphology of bacterial biofilms treated with the optimized formulations was examined by scanning electron microscopy with the MA-1518: Carl Zeiss microscopy Pvt. Ltd. In every 12-well-culture plate, wells containing a spherical cover glass-slip, bacterial cell culture (500 µL) in the logarithmic phase and varying concentrations (500 µL) of the test agents (optimized formulations, 500 µL) were added. Coverslips were then rinsed with PBS and subsequently fixed in a glutaraldehyde solution (2.5%) for 3 hr at 4°C. Before fixation, the coverslips were subjected to incubation for 24 hr at 37°C. Following biofilm formation on the coverslips, dehydration was carried out for 10 min. at 4°C using an ascending ethanol percentage series of 25%, 50%, 70%, 90% and 100%. Before SEM investigation, the cover glass-slips were thoroughly evaporated and covered with a protective carbon layer via sputter coating.

5.2.2.6. Assessment of live and dead cell viability

The microbial viability test was conducted using confocal laser scanning microscopy to differentiate between Living and dead microbial cells, employing the LIVE-DEAD microbial Bac Light viability/visibility kit. The staining solution was applied using one of the 3 approaches: (i) directly onto biofilm-coated surfaces, here the stain mixture was diluted in PBS, then applied to the biofilm using a micropipette and covered using

coverslip; (ii) microbial cells detached from outer surfaces via ultrasonication; (iii) microbes harvested from superficial biofilms layer. Stained samples were preserved in darkness at room temperature for a duration of 15 minutes.

5.2.2.7. TEM analysis of microorganisms

TEM is a powerful analytical approach employed to investigate the morphological attributes, intracellular organization, and microbial-interactions within the environment. Microbial cells from the untreated group (control) and those exposed to G-S-CMC-Pep-NPs (at the concentration optimized for the specific microorganism) were rinsed twice with buffer PBS of pH 7.4 and subsequently 2.5% (v/v) of glutaraldehyde was used for fixation, followed by fixation with 1% osmium tetroxide was done. Cells were subsequently rinsed again with buffer PBS of pH 7.4 before undergoing gradual dehydration using an increasing ethanol gradient. Ultrathin sections were obtained using an ultramicrotome (Leica UC-7) fitted with a diamond knife and were mounted on copper grids. These sections were then immediately analyzed using cryogenic TEM (CRYO-TEM, ThermoScientific) at an operating 80 kV voltage.

5.2.3. Hemolysis analysis

Evaluating the hemolytic activity is critical for establishing the safety profile of nanoparticles for wound dressing applications, distilled water, saline, G-NPs, S-NPs, G-S-NPs, G-S-CMC-NPs and G-S-CMC-Pep-NPs were taken for comparative test. Blood samples were collected from a group of healthy mice, thereafter plasma was isolated through centrifugation, and the cell pellet was then subjected to three rinses with PBS. A total of 200µL of the rinsed blood was mixed with 800µL of each formulation samples. All tubes were then incubated for 3 hr at 37°C and subsequently centrifuged at 5000 rpm for 10 min. After centrifugation, 100µL of supernatant was transferred to 96-well plates, and

absorbance was recorded at a wavelength of 540 nm. The percentage of hemolysis was calculated using the equation 1:

$$\%\ Hemolysis = \frac{Optical\ density\ of\ test - Optical\ density\ of\ PBS}{Optical\ density\ of\ distilled\ water - Optical\ density\ of\ PBS} X\ 100 \quad (1)$$

5.2.4. Fabrication and evaluation of G-S-CMC-Pep-NPs-NFs

10% (w/v) chitosan (CH) was dissolved to prepare chitosan solution in a binary solvent composed of water and acetic acid in an 80:20 ratio at 90°C, utilizing stirrer. Additionally, PVA solution at 7% (w/v) concentration was prepared by dissolving PVA in distilled or deionized water under consistent parameters and maintaining a consistent 90°C temperature. The CH (10 wt.%) and PVA (7 wt.%) liquid solution was formulated by mixing equal volumes of the CH-PVA solutions were in a 1:1 [145]. Furthermore, G-S-CMC-Pep-NPs solution (2.5 mL) was integrated with CH-PVA viscous solution (4 mL). Mixture of CH-PVA-G-S-CMC-Pep-NPs was intensely agitated for 3 hours. The resulting homogeneous gel was then utilized for drop-casting or electrospinning processes.

5.2.4.1. Electrospinning

In a standard electrospinning protocol, solution of CH-PVA-G-S-CMC-Pep-NPs was loaded within a syringe delivery system and electrospun at voltage of 15 kV. The proximity from the needle tip to the collection target was maintained at 15 cm, with aluminum foil serving as collection plate. The rate of flow was kept constant at 0.5 mL/h, revolving cylinder was calibrated to 6000 rpm, followed by electrospinning was started to perform for a period of 3 hours [146].

5.2.4.2. Contact angle analysis

A "First-Ten-Angstroms" device manufactured in Portsmouth, Virginia, USA, was used to measure the water contact angle. Placing 1x1 cm electrospun nanofiber membrane samples on a plate, we sprayed them with distilled or deionised water [122, 147]. The contact angle

calculations based on cameras were used to assess for the blank and G-S-CMC-Pep-NPs-NFs nanofibers.

5.2.4.3. Fourier transform infrared investigation

Fourier Transform Infrared (FT-IR) analysis was utilized to analyze the presence of different functional groups on electrospinning nanofibers, employing a Nicolet iS-5 (THERMO-Electron Scientific-LLC).

5.2.4.4. X-ray-diffraction analysis

X-ray-diffraction (XRD) analysis of the electrospinning nanofibers was executed utilizing a Bench-Top XRD from RIGAKU-Corporation.

5.2.4.5. Evaluation of nanofiber by TEM

For investigation utilising a FE-TEM (Technai G-2 20-TWIN), nanofibers were placed onto TEM copper grids in a co-axial arrangement.

5.2.4.6. Evaluation of nanofiber by SEM

After the nanofibers were coated with carbon sputtering, their morphology and configurations were examined using a field-emission scanning electron microscope (EVO SEM MA-15/18, Carl Zeiss Microscopy Pvt. Ltd.).

5.2.4.7. Evaluation of nanofiber by AFM

Morphology and topography of the electrospinning nanofibers were examined with NTEGRA-Prima system from NT-MDT-Service Logistics Pvt. Ltd. Nanofiber's solution droplets were subjected to vacuum drying on mica substrates overnight prior to scanning in Asyst-peak force-tapping mode in atmospheric air. The AFM employs a mode of scanning that features a silicon-cantilever positioned vertically alongside the sample.

5.2.4.8. Water-retention capability

To evaluate water retention capacity of the nanofibers, they were immersed in a PBS buffer solution of pH 7.4 at 37°C for 48 hours. At specified time frames, the samples were

extracted from the solution, gently dry with soft paper, and weight was measured using a high-accuracy electronic balance [148, 162]. Each sample was tested in triplicate. The percentage of water retention was determined according to equation 2:

$$Water\ retention\ (\%) = \left(\frac{Wwet - Wdry}{Wdry}\right) X\ 100 \qquad (2)$$

Where, W_{wet} and W_{dry} represent the weights of the wet and dry samples, respectively

5.2.4.9. Nanofibers' stability and degradation

Nanofibers were examined for stability and degradation of the by soaking the nanofibers sheet in a PBS buffer media of 7.4 pH and a lysozyme (120 U/mL in distilled water) solution at 37°C. Lysozyme degradation was assessed over a period of 20 days; the lysozyme solution being replaced by fresh solution of lysozyme for every 2 days. On the day 10 and 20, the nanofibers were removed from the solution and rinsed twice with water [148]. Equation 3 was to calculate the percentage rate of degradation is expressed as follows:

$$Degradation\ (\%) = \left(\frac{Wi - Wf}{Wi}\right)\ X\ 100 \qquad (3)$$

Where, W_i and W_f represent the sample weights prior to and following degradation, respectively.

5.2.4.10. *In vitro* release profile

In vitro release profile was done with the diffusion method (dialysis bag) employed to evaluate the release kinetics of gold and silver ions through the synthesized G-S-CMC-Pep-NPs and G-S-CMC-Pep-NPs-NFs. Specifically, 1mL, of G-S-CMC-Pep-NPs were enclosed in a dialysis kit comprising of 1 kDa molecular mass-cut-off and tightly packed. For the G-S-CMC-Pep-NPs-NFs, the nanofibers were cut into smaller pieces measuring 1x1 cm (approx.), with around 10 mg submerged in 1 mL PBS buffer solution of pH 7.4 at 37°C. Samples were then also placed in a dialysis bag of 1kDa and sealed tightly. Dialysis

kit was then immersed in a glass-flask containing PBS (100 ml) comprised buffer solution of pH 7.4. Entire setup was placed in a water-bath shaker (Remi CM12+, Vasai) maintained at 37 ± 1°C, ensuring continuous shaking throughout the experiment [149]. At predefined time periods of 1h, 2h, 3h, 6h, 8h, 12h, 24h, and 48 h, 1 mL sample was withdrawn from both, and an identical volume of freshly prepared buffer medium was added to maintain the sink conditions. Samples were then analyzed using UV visible spectroscopy at wavelength 517 nm. Unknown sample concentration in a compound was calculated utilizing a predefined standardized calibration graph (R^2 = 0.9915) specifically to the bi-metallic compounds.

5.2.4.11. Nanofibers' hemolysis

Nanofibers underwent a hemolytic analysis to evaluate their safety for human use. This assay measured the capacity of erythrocytes (red blood cells) to lyse and hemoglobin release into the plasma. Based on their hemolysis index, dressings are classified into three categories according to ASTM F 756-00 (2000): (i) Hemolytic dressings exhibit a hemolysis percentage exceeding 5%, (ii) dressings with a moderate hemolytic impact are defined by a hemolysis percentage between 2% and 5%, and (iii) the dressing in question is classified as non-hemolytic, indicated by index of hemolysis of less than 2% [151]. The hemolytic impact of nanofibers was evaluated in G-S-CMC-Pep-NPs-NFs compared to distilled or deionized water, and saline

5.2.4.12. Blood clotting study

The nanofibers' haemostatic properties were tested by placing individual films in pre-heated, 37°C glass petri dishes[152]. Following this, 200µL of freshly drawn human blood was exposed to each film surface, followed by addition of 30µL of 0.2 M $CaCl_2$ to begin the procedure of coagulation. The petri-dishes contains the nanofibers were subsequently kept for incubation at 10 min. at 37°C. Post-incubations, 30mL of distilled or deionized

water was carefully introduced drop-wise to each petri dish to avoid disturbing the formed clot, facilitating hemolysis of erythrocytes not incorporated within clot, utilizing a total quantity of 25 mL water. Thereafter, hemoglobin solution absorbance was determined at λmax of 540 nm.

5.2.4.13. Thrombus formation study

According to standard protocol, a nanofiber film/sheet (1×1 cm) was submerged in a saline medium at 37°C for 24 hr. Following this, the nanofiber was extracted from the saline medium and subsequently exposed to 2 mL of anticoagulant citrate dextrose blood in which, the solution was meticulously administered on the nanofiber surface. This was done after the addition of 30µL of a 0.2 M $CaCl_2$ medium to initiate thrombus formation, which occurred over a period of approximately 3 to 4 minutes [153]. The thrombus formation was terminated by the exposure of 8 mL of deionized water at 20 min. Afterwards, the clot was submerged in a 40% formalin solution (10 mL) for 10min. Finally, the stabilized clot was thoroughly washed with distilled water, dried gently using blotting paper, and weighed.

5.2.5. Preparation of ultra small magnesium nanoclusters

Ultra small magnesium nanoclusters (USM) were synthesized as a fluorescent agent following the methodology described by Srivastava et al [163], following the established protocol. Initially, all apparatus were cleaned with aqua-regia (HCl (3):HNO_3 (1)) and subsequently washed twice or thrice with deionized water and ethanol. Magnesium chloride solution (10 mM, 10 mL) was mixed with a bovine serum albumin solution (450 mg/mL, 1 mL) to create bovine serum albumin templated magnesium nanoclusters. After 5 min. of mixing at 55°C and 900 rpm, L-ascorbic acid/Vitamin C (35 mg/mL, 3 mL) was administered. The mixture was then held at 55°C with continuous intensive agitation for 3 hours. Following this experiment time, the initially colorless liquid transitioned to a pale-yellow hue. The liquid was then incubated for an additional 15 hours at 55°C, during which

tonal shift from light yellow to pale yellowish occured, signifying that the experiment was complete. Larger particles were separated through centrifugation at 15000 rpm for 10 minutes. Resulting USM solution was then lyophilized and kept at 4°C. The synthesized USM was analyzed for its fluorescence activity and for morphology using TEM.

5.2.6. *In vivo* fluorescence imaging of G-S-CMC-Pep-NPs-NFs

In vivo fluorescence imaging was conducted on nanofibers using free USM (blank) and G-S-CMC-Pep-NPs-NFs tagged with USM on both non-infected and various bacterial wound infections in animals, utilising Biospace Lab's photon imager optima system. Treatments, comprising free USM and USM-labeled G-S-CMC-Pep-NPs-NFs comparable to 100 nM of USM nanoclusters, were exposed directly to the wounds. Followed by capturing fluorescence signals of 469 nm (excitation) and 543 nm (emission) wavelengths, at 10 min post-exposure and at subsequent period of 2 h, 4 h, 8 h, 24 h, and 48 h.

5.2.7. Wound healing investigation

5.2.7.1. *In vivo* wound healing investigation

A study investigating wound recovery efficacy was conducted using Swiss albino mice weighing between 18 and 22 grams. All *in vivo* animal research granted endorsement from Institutional Animal Ethics Committee (IAEC) of Indian Institute of Technology (IIT-BHU) located in Varanasi, UP, India (IAEC grant number- IIT (BHU)/IAEC/2023/II/032) and the experiment was performed in accordance with the protocols established by the National Research Council guide for care and use of laboratory animals. The mice were kept in a monitored condition with controlled temperature, consistent level of humidity, and a 12-hour dark/light cycle. A total of five random mice were allocated to 7 distinct groups. An Excision-induced wound paradigm was created by initially applying depilatory cream to the dorsal region, and then shaving was done. After administering ketamine (50 mg/kg bw, IP) to induce sedation in the mice, a circular wound approximately 280 mm^2 in

size was excised. The wounds of each group of five mice were intentionally exposed to the respective MDR bacteria to the lesion sites. For the positive control here, a market-available ciprofloxacin ointment, recognized for its broad-spectrum antibiotic properties, was applied. In contrast, the negative control group consisted of lesions has received no treatment. Additionally, one cohort was kept free from infection while receiving therapy with G-S-CMC-Pep-NPs-NFs. Moreover, various demographic-cohorts were subjected to infections from different MDR bacterial strains. The test animals were categorized into the following groups:

Group 1: No treatment was administered to the mice's wounds

Group 2: Wounds in the murine model were subjected to ciprofloxacin therapy, USP, at a concentration of 0.3% (w/w);

Group 3: The murine wound model was kept free of infection and administered with G-S-CMC-Pep-NPs-NFs at a concentration of 0.390 μg ml−1;

Group 4: Wounds in the murine model were infected through inoculation with MDR *P. aeruginosa* at the wound sites, after which therapy with G-S-CMC-Pep-NPs-NFs was applied at a concentration of 0.390 μg ml^{-1};

Group 5: Wounds in the murine model were infected by inserting multidrug-resistant *S. aureus* bacteria into the wound. Subsequently, the wounds were treated with a solution containing G-S-CMC-Pep-NPs-NFs at a concentration of 0.781 μg ml−1.

Therapies were applied daily from the initiation of the procedure until the conclusion of the regeneration phase. ImageJ software was employed to statistically evaluate wound healing by comparing the area of wound at specific time interval with the first day wound area. The relative percentage of the wound region was graphed against time to elucidate the rate of recovery.

5.2.7.2. Histopathological studies

After a 12-day observation period, the mice in every group was euthanized via CO_2 hypoxia. Subsequently, the tissue layers containing the wounds were meticulously excised, processed tissues were retained in a 10% (v/v) formalin solution. Tissue samples were then sectioned into 10 µm thick tissue sections were obtained utilizing a rotary microtome and subsequently subjected to hematoxylin and eosin staining to enable comprehensive histopathological analysis. Histological changes were observed using a Dewinter microscope (bright field microscope) in conjunction with a software Capture Pro-4.1 [154].

5.2.8. Live ultrasound/photoacoustic investigation

The infected wound model established following infection with isolated MDR bacteria, was utilized for the *in vivo* photoacoustic imaging studies. The animals were subsequently allocated into seven cohorts, with every group comprising three individuals (n=3). Following this, all subjects underwent scanning using a photoacoustic imaging instrument (model-Vevo-LAZR-X-Vevo-3100, Toronto-Canada at 40 MHz array-transducer ultrasound). Wounds were assessed using B-mode approach of ultrasound imaging, with the power doppler approach activated for vascularity analysis and the photoacoustic approach employed to differentiate between oxygenated and deoxygenated blood. Imaging was conducted on the 1^{st}, 4^{th}, 8^{th} and 12^{th} day following therapy, allowing for a comprehensive visualization of the wound's characteristics. The ultrasound and photoacoustic results were overlaid to evaluate the wound's size and oxygen saturation levels (% sO2). Additionally, the power doppler imaging mode was utilized to assess vascular density. Image processing was performed using Vevo LAB software[155].

5.2.9. Western blotting analysis

The western blotting technique was employed to study the expression of the signaling receptor EGFR, phosphorylation of its component ERK 1/2, and mesenchymal tissue

marker Vimentin related with epithelial-mesenchymal-transition (EMT). Skin's wound tissues of mice with no treatment, treatment with marketed formulation, and bacterial infected wound (MDR isolated *P. aeruginosa*, and MDR isolated *S. aureus*) treatment with G-S-CMC-Pep-NPs-NFs were sectioned on ice. Using an electric homogenizer, an estimated 5.0 mg of skin tissue underwent homogenization in 250-300µl of frozen ice 1X RIPA lysis buffer (50mM Tris-HCl of pH-7.4, 1% NP- 40, and 0.25% sodium-deoxycholate, 150mM NaCl, and EDTA-1mM). The protein content was quantified by nano-drop (ThermoScientific) and samples having approximately 75.0 µg of proteins were denaturized and run at 12% sodium-dodecyl-sulfate-polyacrylamide-gel-electrophoresis (SDS-PAGE). After separating peptides using SDS-PAGE, proteins moved from the gel to a membrane made of PVDF and left to overnight. After blocking the membrane with a 4% milk skimmed solution in TBST, it was then incubated with the antibody (primary) was applied, incubating with an antibody (secondary) employed to alkaline phosphatase. Signal detection was performed using FAST-NBT-BCIP-Sigma for chromogenic visualization. Primary antibodies employed in the western-blotting includes Rabbit anti-Vimentin, Rabbit anti-EGFR, Rabbit anti-Phospho ERK-1/2, and Rabbit anti-beta-Actin. Vimentin levels were markedly enhanced in samples of protein derived from MDR *P. aeruginosa* infected mice exposed with G-S-CMC-Pep-NPs-NFs, relative to a group of control animals with no treatment.

Similarly, EGFR and phosphorylation of ERK 1/2 responsible for inducing EMT were also found to be upregulated, as demonstrated by the elevated expression of EGFR and p-ERK 1/2 in these protein samples. The exposure of G-S-CMC-Pep-NPs-NFs resulted in a modest elevation of these EMT markers in both uninfected and mice infected with other microbes. This indicates that the G-S-CMC-Pep-NPs-NFs developed in-house in our laboratory

augmented wound healing process in animals infected with MDR *P. aeruginosa*. The band intensity of the proteins were analyzed using ImageJ.

5.2.10. Statistical interpretation

Comprehensive *in vitro* and *in vivo* data were analyzed with software GraphPad Prism 9.0. All experiments setups were performed in a triplicate manner, with data presented as mean± standard deviation (SD). Statistical significance between groups was determined using t-test. The degree of significance was determined using the following values: ns ($p \geq 0.05$), * ($p < 0.05$), ** ($p < 0.01$), *** ($p < 0.001$), and **** ($p < 0.0001$).

5.3. Results

5.3.1. Characterization of nanoparticles

5.3.1.1. Size of the nanoparticles, PDI and zeta potential

The synthesized nanoparticles exhibited a particle size ranging from 46.8 ± 2.0 nm to 155.1 ± 11.2 nm, whereas the PDI were in the range of 0.101 ± 0.035 to 0.216 ±0.079 and the associated surface charge was in the range of 17.7 ± 1.3 mV to 34.6 ± 3.7 mV respectively **(Table 5.2. and Figure 5.3.)**. The outcomes demonstrated that evenly distributed G-S-CMC-Pep-NPs demonstrated a greater positive charge compared to their bimetallic and monometallic counterparts.

Table 5.2. PS, PDI and zeta potential of the synthesized nanoparticles

Nano-formulation	Particle size (nm) (Mean ± SD)	Polydispersity index (Mean ± SD)	Zeta potential (mV) (Mean ± SD)
G-NPs	46.8 ± 2.0	0.169 ±0.034	17.7 ± 1.3
S-NPs	89.4 ± 3.9	0.116 ±0.088	19.1 ± 2.4
G-S-NPs	92.6 ± 6.1	0.216 ±0.079	21.8 ± 2.8
G-S-CMC-NPs	119.3 ± 8.5	0.101 ± 0.035	23.2 ± 4.1
G-S-CMC-Pep-NPs	155.1 ± 11.2	0.133 ± 0.052	34.6 ± 3.7

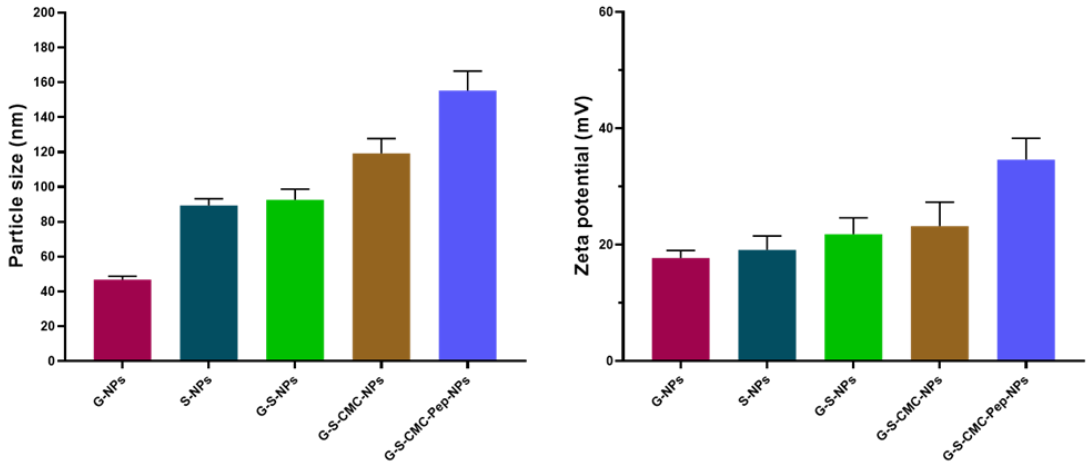

Figure 5.3. Particle size and zeta potential of the synthesized nanoparticles

5.3.1.2. TEM analysis

TEM analysis of the optimized formulations were carried out at resolutions ranging from 40 nm to 300 nm. Morphology of G-NPs, S-NPs and G-S-NPs displayed a distinctive circular form devoid of any coating. Conversely, TEM results of G-S-CMC-NPs and G-S-CMC-Pep-NPs indicated the presence of an additional surface layer, suggesting the successful deposition of CMC and LL-37 on the nanoparticle surface **(Figure 5.4.)**. The physical characteristics of the synthesized nanoformulations were evaluated through SAED pattern (Selected area electron diffraction) analysis. SAED pattern of G-NPs exhibited a well-defined arrangement of bright regions, indicative of a crystalline structure. In contrast, the SAED patterns of S-NPs, G-S-NPs, G-S-CMC-NPs, and G-S-CMC-Pep-NPs demonstrated irregularly distributed discrete circular patterns and points, signifying polycrystalline morphology.

5.3.1.3. AFM analysis

Morphology of surface of the optimized formulations were characterized using AFM **(Figure 5.4.)**. The formulations exhibited a smooth surface texture, spherical shape and an absence of any detectable pinholes or surface fractures.

5.3.1.4. EDS analysis

The G-S-CMC-Pep-NPs were subjected to investigation including mapping and spectrum using EDS to identify and quantify gold and silver in the nanoformulation's core. **Figure 5.5.** presents mapping and spectrum of the elemental composition, indicating that silver and gold constitute 81.60% and 18.40%, respectively.

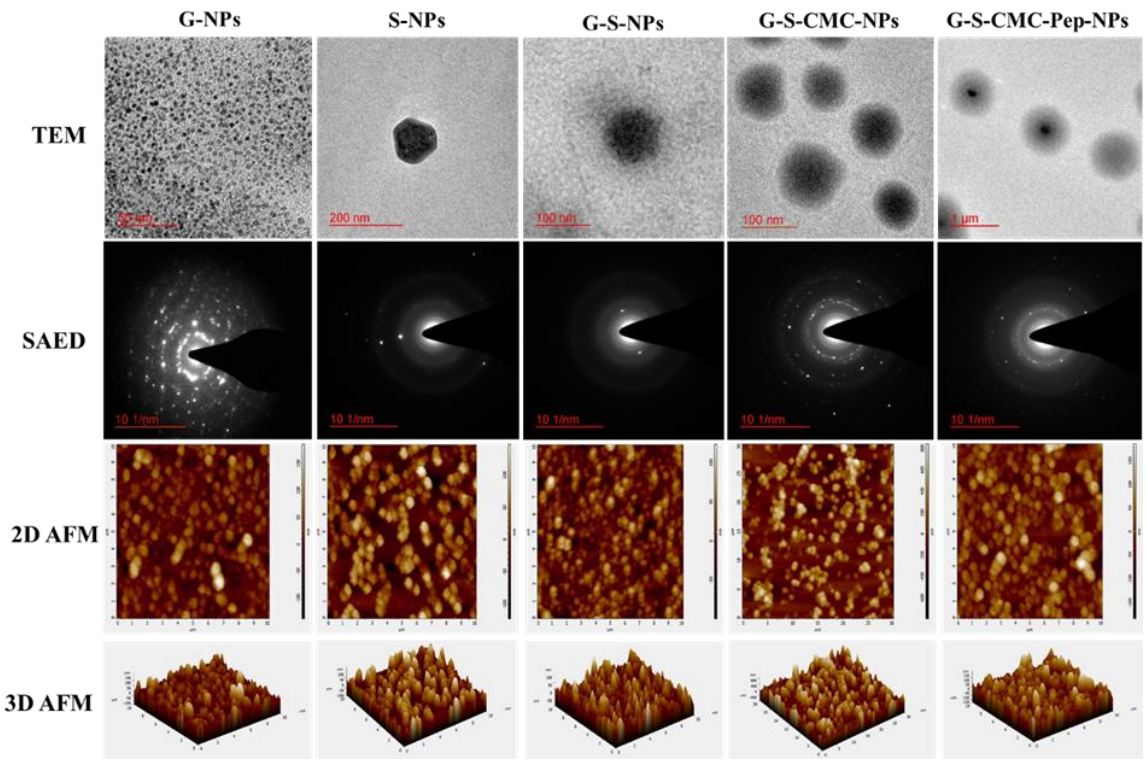

Figure 5.4. HR-TEM, SAED, 2D AFM, and 3D AFM of the optimized nanoformulations

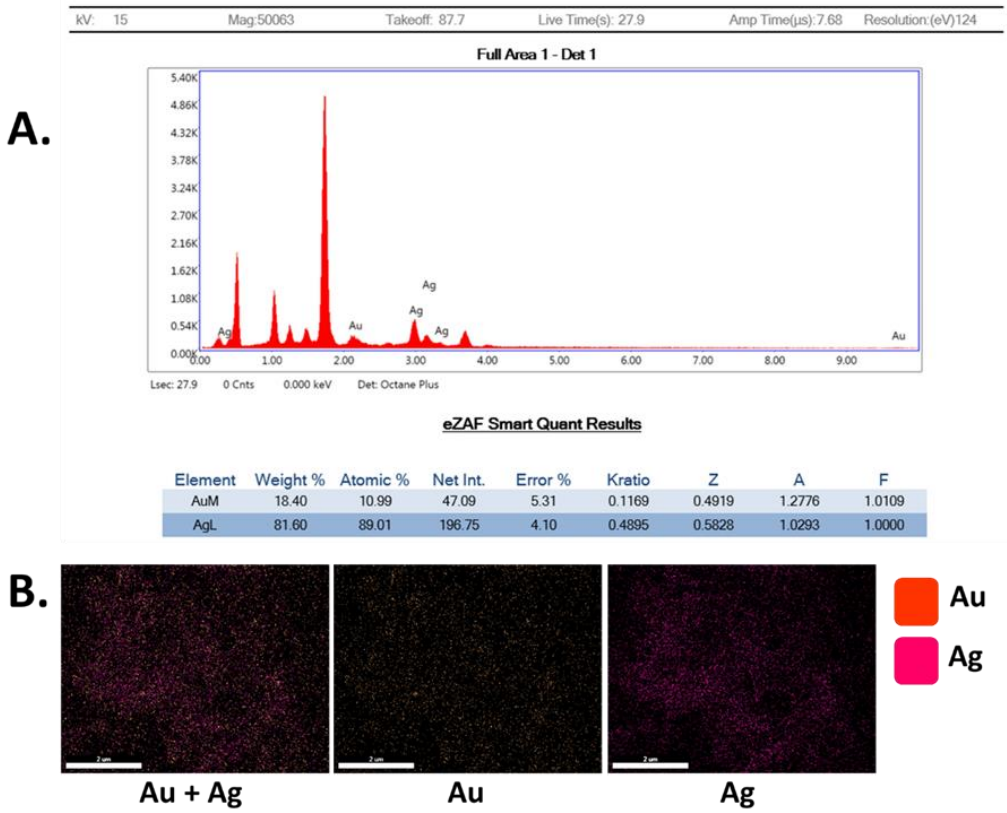

Figure 5.5. The EDS elemental analysis of G-S-CMC-Pep-NPs

5.3.2. Antibacterial potential of nanoparticles

5.3.2.1. Prevalence and resistance rate of *P. aeruginosa* and *S. aureus*

A total of 33 environmental wastewater samples were analyzed to detect the prevalence of drug-resistant bacterial isolates. Out of these, 87% tested positive for one or more bacterial isolates. In total, 76 distinct bacterial isolates were recovered from the samples **(Figure. 5.6.)**. Most frequently isolated bacterium was *P. aeruginosa* - 36 (47.36%) followed by *S. aureus* - 22 (28.94%) and other isolates were 18 (23.68%). In other aspect, down-stream water has total of 21 bacterial isolates out of which *P. aeruginosa* -11 (52.38%), *S. aureus* - 6 (28.57%) and other isolates were 4 (19.04%); ICU has total of 18 bacterial isolates out of which *P. aeruginosa* -7 (38.88%), *S. aureus* - 5 (27.77%) and other isolates were 6 (33.33%); Pathology lab has total of 15 bacterial isolates out of which *P. aeruginosa* -5

(33.33%), *S. aureus* -5 (33.33%) and other isolates were -5 (33.33%); Surgical ward has total of 10 bacterial isolates out of which *P. aeruginosa* - 6 (60.00%), *S. aureus* -3 (30.00%) and other isolate was -1 (10%); and water cooler sink has total of 12 bacterial isolates out of which *P. aeruginosa* - 7 (58.33%), *S. aureus* -3 (25.00%) and other isolates were -2 (16.66%).

Antibiotic sensitivity tests **(Figure. 5.6.)** revealed that *P. aeruginosa* isolates were resistant to amoxicillin (10 µg) 92.30%, doxycyline (15 µg) 66.66%, clarothromycin (5 µg) 53.84%, cefuroxime (10 µg) 38.46%, metronidazole (5 µg) 33.33%, cephalixin (20 µg) 28.20%, ciprofloxacin (5 µg) 28.07, sulfamethoxazole (5 µg) 17.94% and chloramphenicol (30 µg) 5.26%. Whereas, *S. aureus* isolates were resistant to amoxicillin (10 µg) 74.37%, doxycyline (15 µg) 69.81%, clarothromycin (5 µg) 57.96%, cefuroxime (10 µg) 29.26%, metronidazole (5 µg) 15.45%, cephalixin (20 µg) 11.29%, ciprofloxacin (5 µg) 21.58%, sulfamethoxazole (5 µg) 9.44% and chloramphenicol (30 µg) 3.15%.

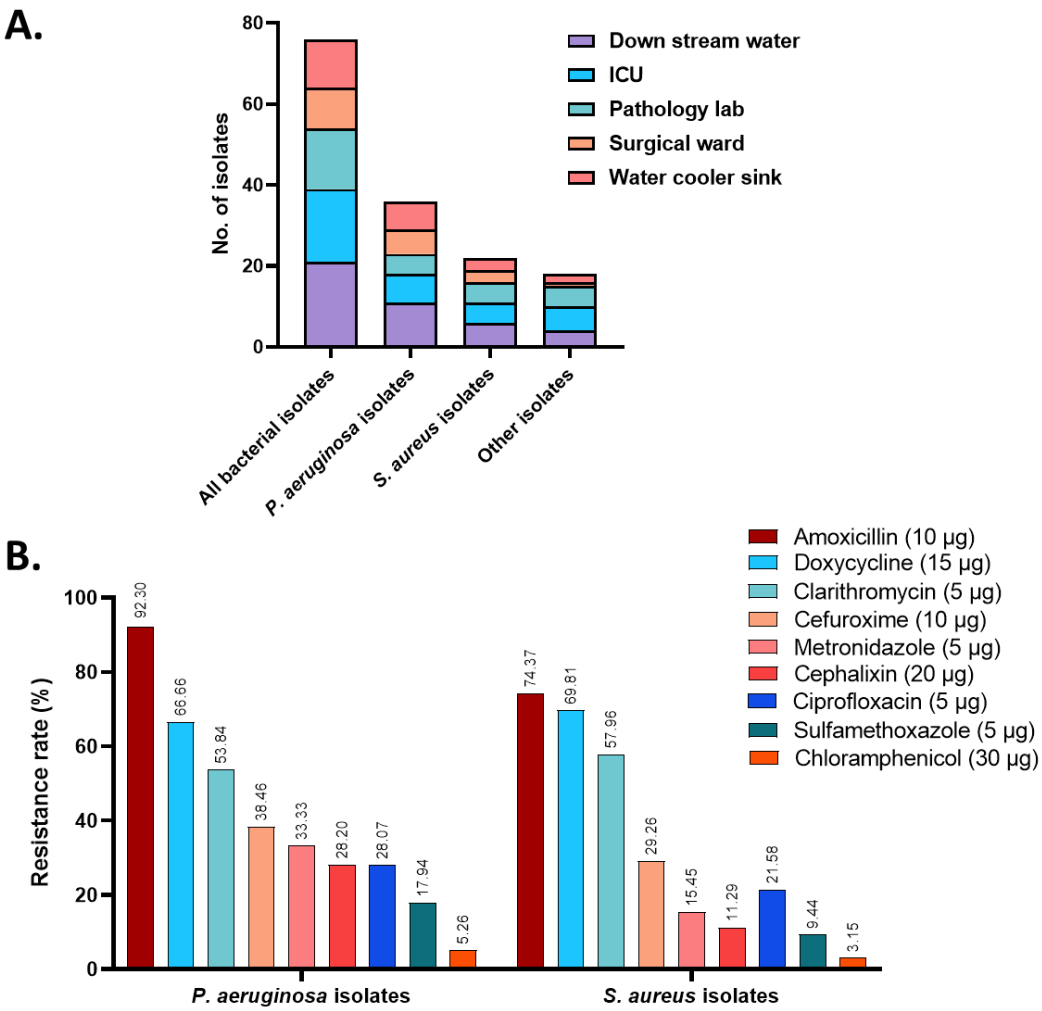

Figure. 5.6. Number of bacterial isolates and percentage of resistance rate

5.3.2.2. MIC and MBC

To investigate the impact of near-MIC treatment on bacterial growth, optical density (OD) measurements were performed. **Figure 5.7.** presents the raw OD data at 600 nm for the respective treatments, where the OD signal correlates with bacterial concentration. Based on the MIC and MBC results, the G-S-CMC-Pep-NPs nanoformulation demonstrated superior efficacy against all tested MDR microbial strains compared to other synthesized formulations and the commercial standard. Consequently, this formulation was selected for subsequent experimental investigations. For, G-S-CMC-Pep-NPs, the proportion of MBC

to MIC for MDR isolated *P. aeruginosa* it was 0.390 µg ml^{-1} /0.390 µg ml^{-1} ⩽ 1, whereas for MDR isolated *S. aureus* was 0.781 µg ml^{-1} /0.781 µg ml^{-1} ⩽1. **(Table 5.3. and Figure 5.8.)**. An MBC:MIC ratio of ⩽4 is indicative of a highly potent antibacterial agent [164]. The findings of this research highlight that the optimized formulation, G-S-CMC-Pep-NPs, exhibits enhanced antibacterial activity relative to other formulations, demonstrating notable potential in both the strains.

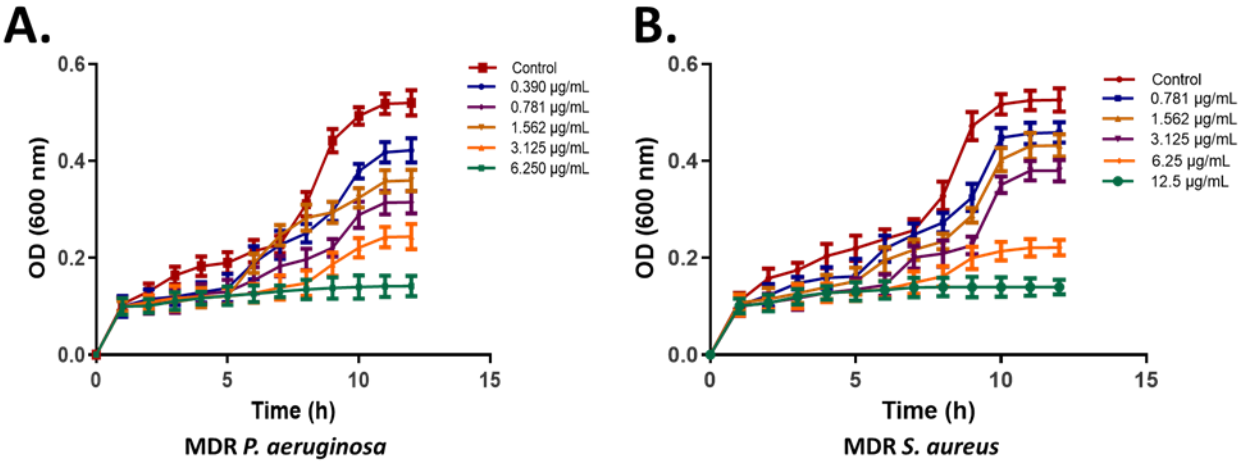

Figure 5.7. Bacterial growth curve A) MDR *P. aeruginosa*; B) MDR *S. aureus*

Table 5.3. MIC and MBC of the optimized formulations

	G-NPs (µg ml^{-1})	**S-NPs (µg ml^{-1})**	**G-S-NPs (µg ml^{-1})**	**G-S-CMC-NPs (µg ml^{-1})**	**G-S-CMC-Pep-NPs (µg ml^{-1})**	**Marketed antibiotic (µg ml^{-1})**
MDR *P. aeruginosa*						
MIC	200	25	12.5	6.25	0.390	0.781
MBC	200	25	25	12.5	0.390	0.781
MDR *S. aureus*						
MIC	100	25	25	12.5	0.781	1.562
MBC	100	50	50	12.5	0.781	1.562

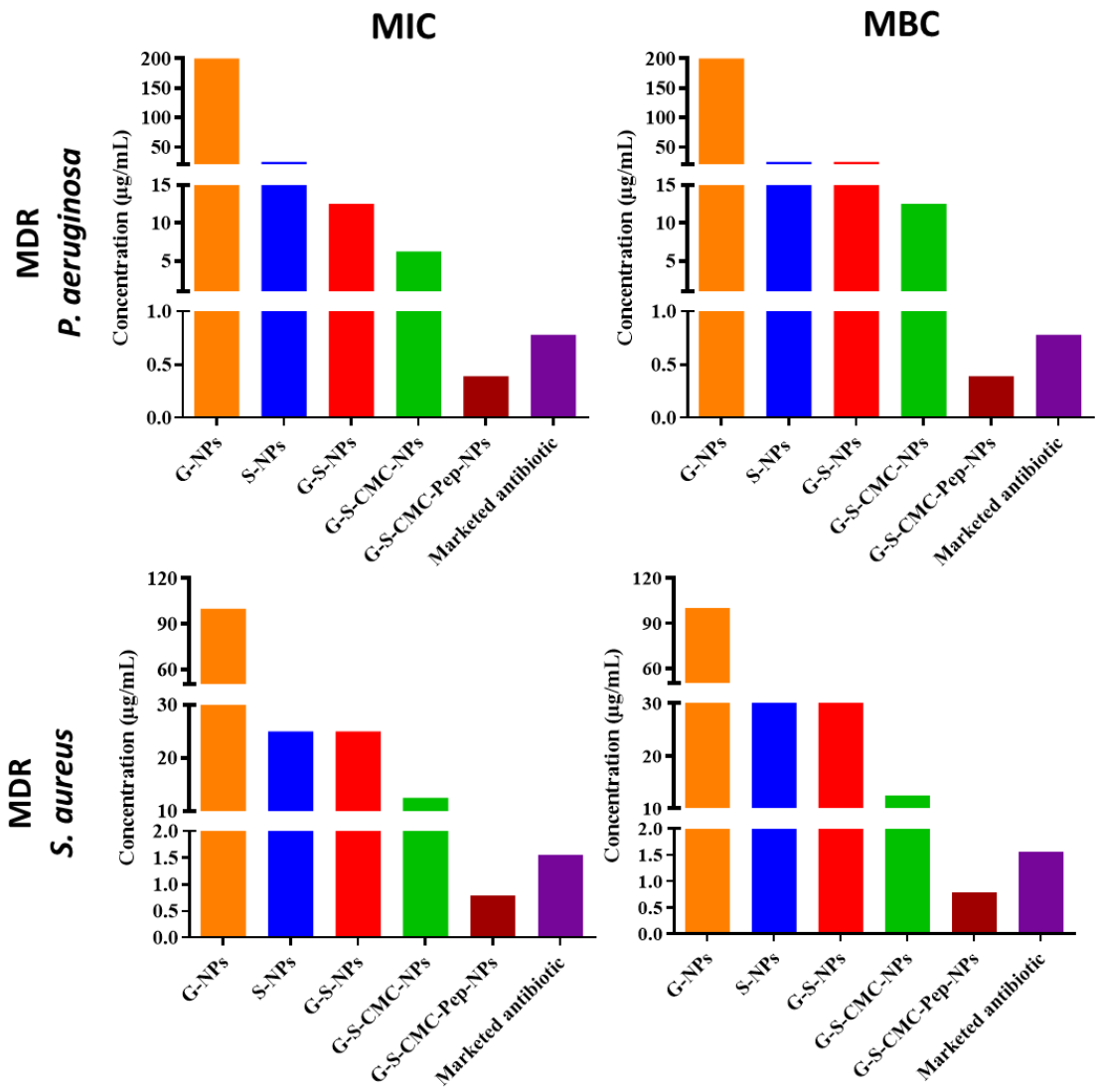

Figure 5.8. MIC and MBC of MDR *P. aeruginosa* and MDR *S. aureus*

5.3.2.3. Bacterial susceptibility

Findings from bacterial susceptibility evaluation revealed G-S-CMC-Pep-NPs exhibited the largest ZOI compared to all other formulations as well as the commercially available ciprofloxacin **(Table 5.4. and Figure 5.9.)**. This study demonstrated that elevating the concentration levels (2 fold) of G-S-CMC-Pep-NPs from 0.390 µg ml^{-1} to 0.781 µg ml^{-1} for MDR *P. aeruginosa*, and 0.781 µg ml^{-1} to 1.562 µg ml^{-1} for MDR *S. aureus*, the ZOI exhibited a modest expansion. This investigation indicates that the synthesized formulation, G-S-CMC-Pep-NPs, exhibits superior antibacterial susceptibility relative to other

formulations. Notably, it demonstrates remarkable potential in targeting MDR *P. aeruginosa* and MDR *S. aureus*.

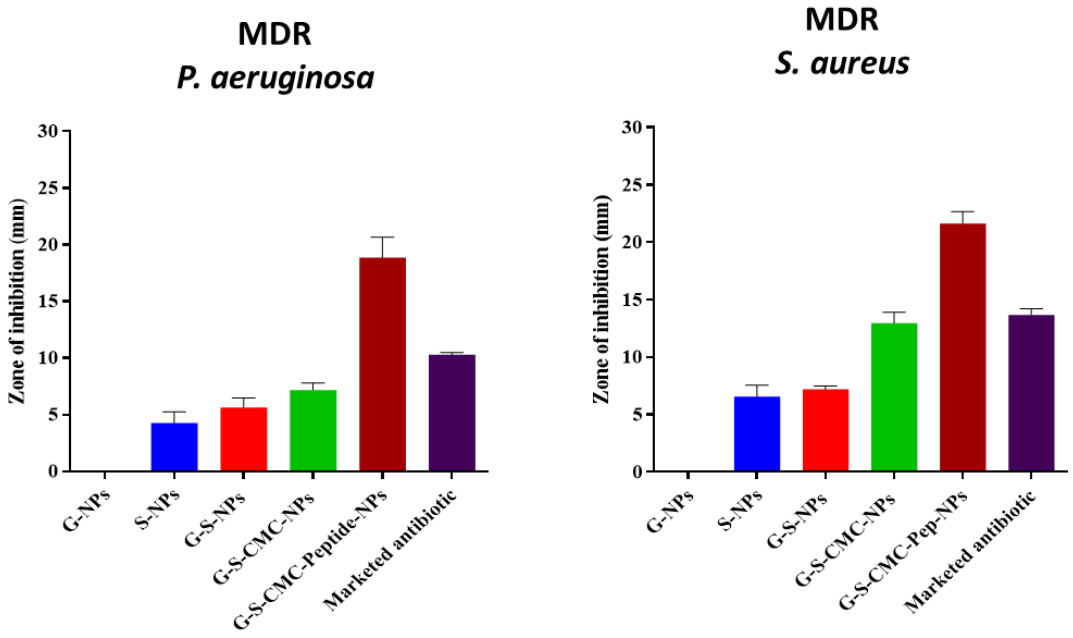

Figure 5.9. Zone of inhibition of MDR *P. aeruginosa* and MDR *S. aureus*

Table 5.4. ZOI of the optimized formulation against multidrug-resistant microbes

	MDR isolated *P. aeruginosa*		**MDR isolated *S. aureus***	
Formulation	**MIC (µg/ml)**	**ZOI (mm)**	**MIC (µg/ml)**	**ZOI (mm)**
G-NPs	200	No zone	100	No Zone
S-NPs	25	6.55 ± 1.02	25	4.28 ± 0.97
G-S-NPs	12.5	7.18 ± 0.31	25	5.63 ± 0.84
G-S-CMC-NPs	6.25	12.94 ± 0.96	12.5	7.16 ± 0.63
G-S-CMC-Pep-NPs	0.39	21.61 ± 1.06	0.781	18.85 ± 1.22
Marketed antibiotic	0.78	13.67 ± 0.54	1.562	10.29 ± 0.19

5.3.2.4. Bacterial viability analysis

Bacterial viability was evaluated using a live-dead approach, after exposing with G-S-CMC-Pep-NPs and the results demonstrated that at 0 hr, the percentage of live cells for MDR isolated *P. aeruginosa* **(Figure 5.10.)** were 72.25 ± 3.61%, however, post 6 hr, and 12 hr exposure, they were determined to be 18.65 ± 0.54% and 3.61 ± 0.13%, respectively. Similarly, the live cells of MDR isolated *S. aureus* **(Figure 5.11.)** were 74.16 ± 4.16% at 0 hr, but after 6 hr, and 12 hr post-treatment, they were determined to be 46.94 ± 2.52% and 11.25 ± 1.91%, respectively. The assessment of viable and non-viable cells in the respective CLSM images was conducted utilizing the ImageJ software, as illustrated in **Figure 5.10. and Figure 5.11**. The augmented antibacterial efficacy of gold silver nanoformulations may be attributed to the elevated free surface energy of the exposed Ag^{+} ions within the bi-metallic nanoparticle configuration [165]. G-S-CMC-Pep-NPs displayed a marked decrease in viable cell numbers coupled with an elevation in dead cell counts when exposed to MDR bacterial strains, highlighting their potent antibacterial synergy.

5.3.2.5. Anti-biofilm analysis

SEM micrographs of the MDR microbes following exposure to G-S-CMC-Pep-NPs revealed progressive disruption of the biofilm structure over the period of time. Results from the SEM images substantiate that G-S-CMC-Pep-NPs possess pronounced anti-biofilm activity **(Figure 5.10. and Figure 5.11.**). The observed effects may be linked to increased intrusion of positively charged G-S-CMC-Pep-NPs, which exhibit a greater interaction affinity for biofilm. Findings indicate that the exposure to these nanoparticles results in a time-based reduction in biofilm formation in multidrug-resistant strains. Moreover, G-S-CMC-Pep-NPs demonstrate significant efficacy against MDR microbes

within housed biofilms, proficiently diminishing the resistance rate of sessile bacterial cells to anti-microbial agents.

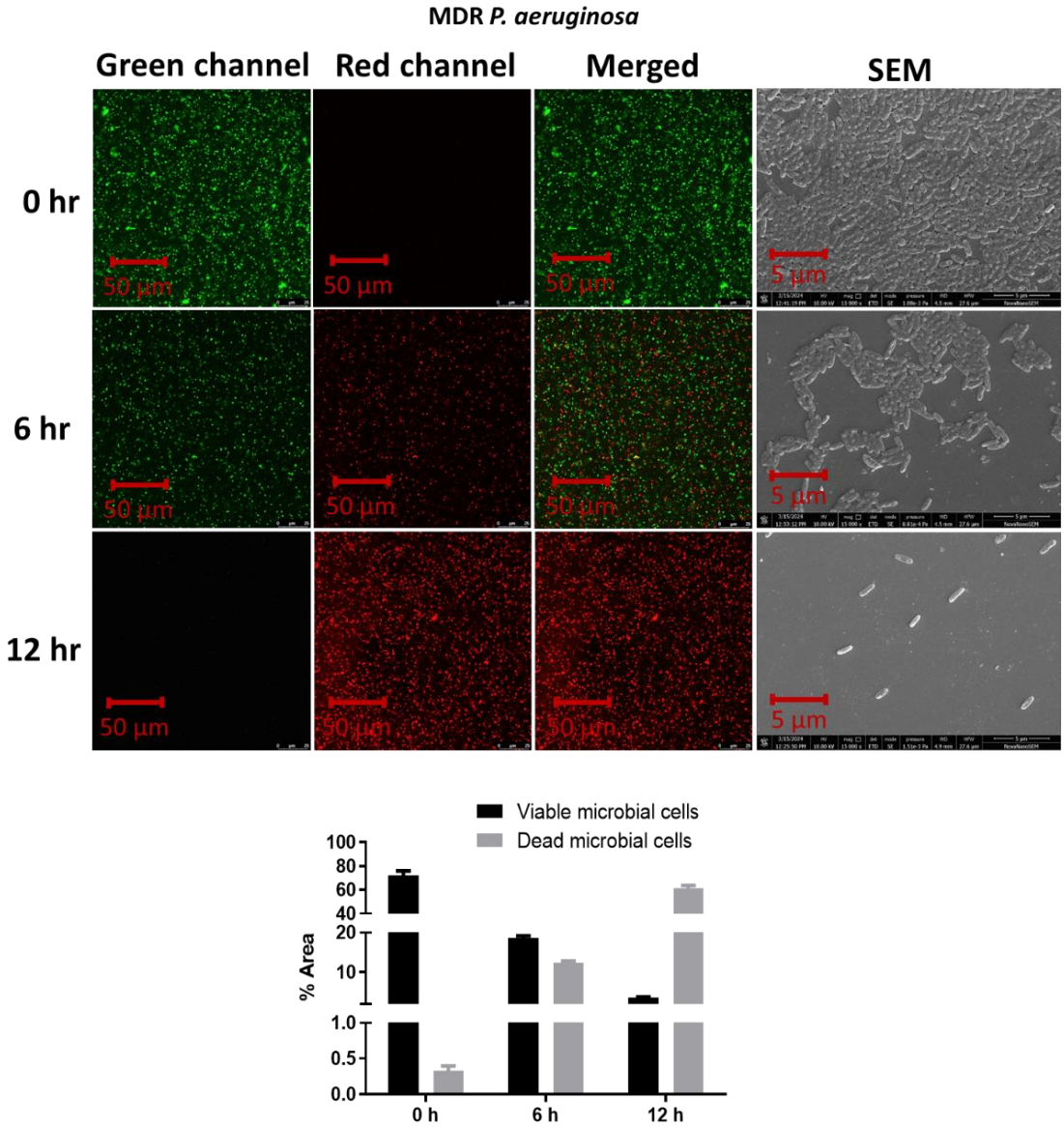

Figure 5.10. CLSM imaging and viable count of multidrug-resistant *P. aeruginosa* following exposure to G-S-CMC-Pep-NPs.

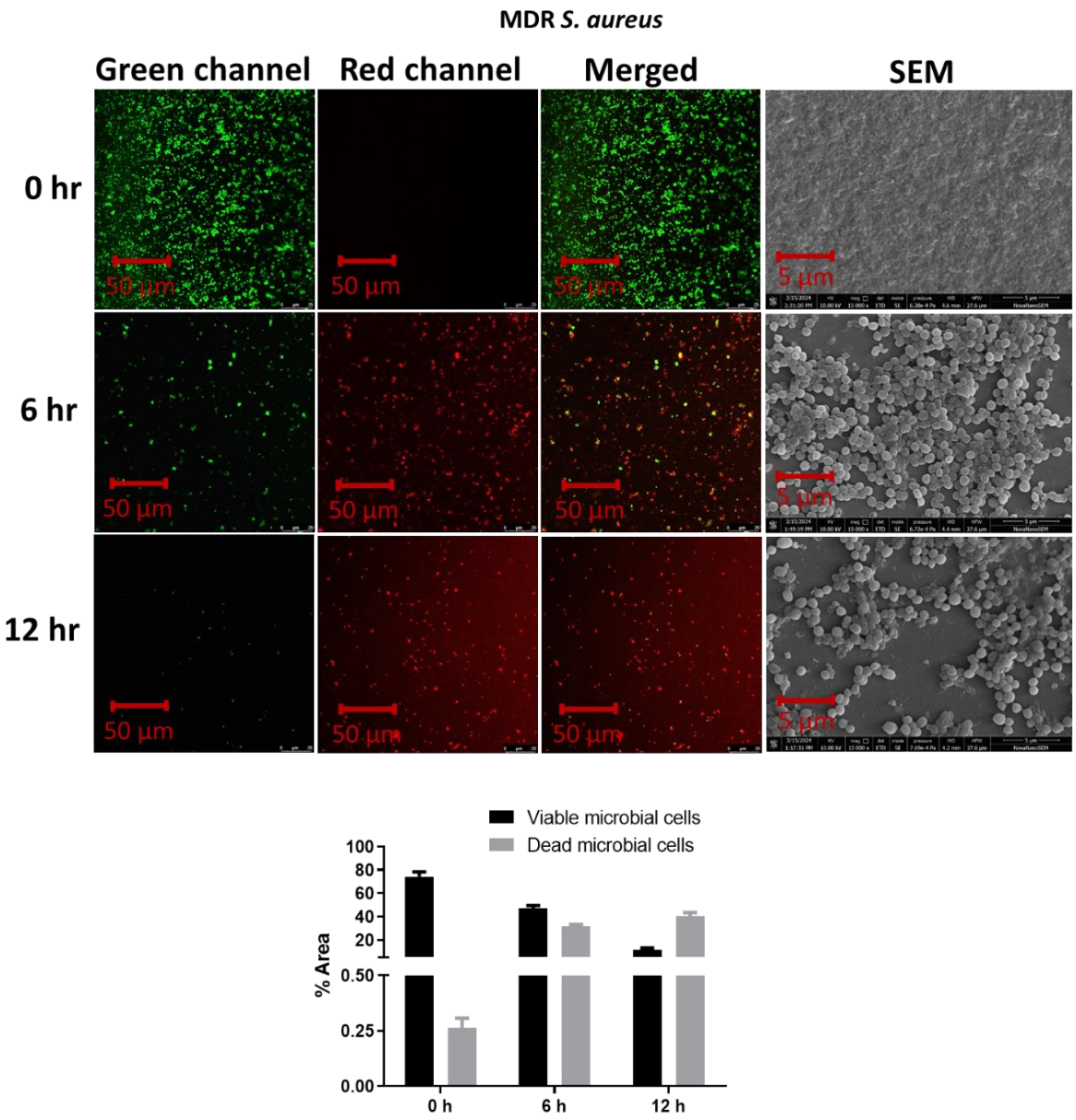

Figure 5.11. CLSM imaging and viable count of multidrug-resistant *S. aureus* following exposure to G-S-CMC-Pep-NPs.

5.3.2.6. TEM investigation of test microorganisms

TEM analysis revealed that G-S-CMC-Pep-NPs exhibited time-dependent anti-bacterial effects against multidrug-resistant bacterial microbes **(Figure 5.12.)**. Initially, at 0 hours, the cell membranes of the MDR microbial strains appeared intact. However, after 12 hours of treatment, TEM images of MDR *S. aureus* indicated significant alterations, including

irregularly wavy and damaged cell walls, resulting in a loss of structural integrity. Comparable findings also were reported in a contemporary investigation. TEM imaging of MDR *P. aeruginosa* unexpectedly revealed no apparent disruption of the outer membrane; instead, it highlighted the DNA condensation within the bacterial organisms [166]. Results of this study indicate that G-S-CMC-Pep-NPs can effectively neutralize multidrug-resistant bacterial strains by compromising cell membrane integrity, disrupting the outer wall, or inducing condensation of bacterial DNA. Further, flow cytometry **(Figure 5.13.)** was performed, by capturing the signals the intensity levels can be more precisely quantified, allowing for better differentiation, provides clear, high-resolution data on bacterial populations.

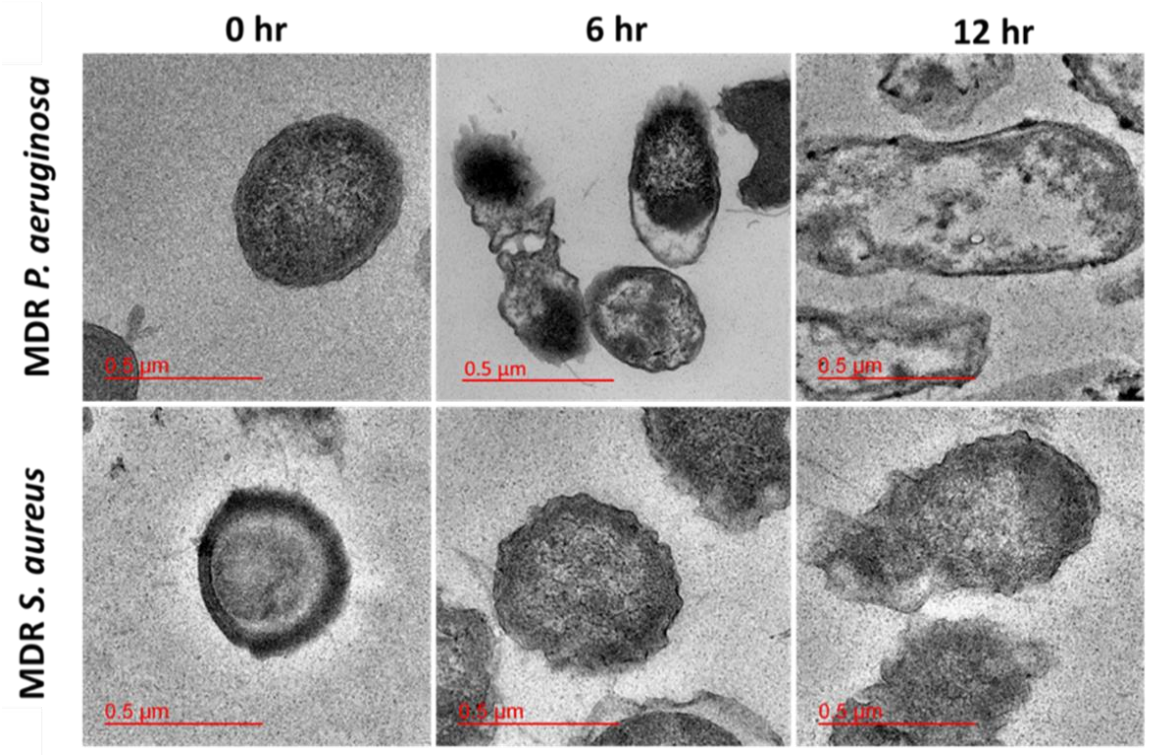

Figure 5.12. TEM analysis of MDR bacterial strains treated by G-S-CMC-Pep-NPs at different time interval at 0hr (control), 6 hr, and 12hr

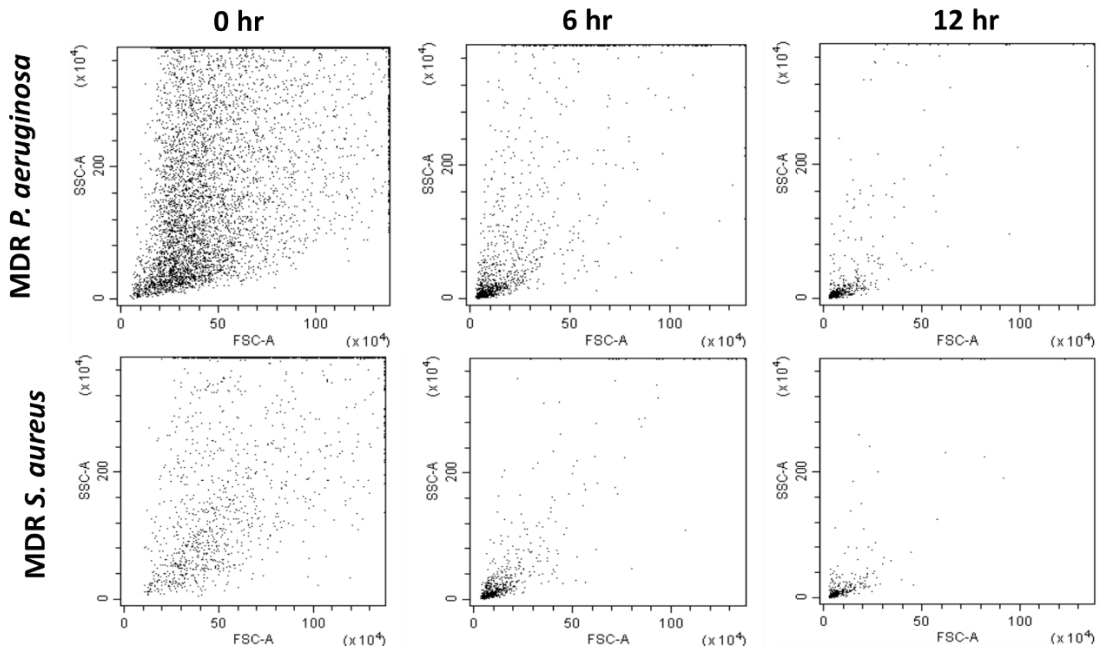

Figure 5.13. Flow cytometry of MDR bacterial strains treated by G-S-CMC-Pep-NPs at different time interval at 0hr (control), 6 hr, and 12hr

5.3.3. Hemolysis analysis of nanoparticles

Hemolytic activity of G-NPs, S-NPs, G-S-NPs, G-S-CMC-NPs, and G-S-CMC-Pep-NPs was evaluated in comparison to distilled or deionized water and saline on RBC, as illustrated in **Figure 5.14.** The hemolytic activity (%) elicited by distilled or deionized water, saline, G-NPs, S-NPs, G-S-NPs, G-S-CMC-NPs, and G-S-CMC-Pep-NPs was 97.65 ± 0.46%, 1.84 ± 0.13%, 3.73 ± 0.60%, 5.98 ± 0.94%, 4.61 ± 0.46%, 4.10 ± 0.59%, and 2.18 ± 0.16% respectively. The results establish that the nanoparticles consistently exhibited hemolysis levels below the established threshold of 2%, confirming their lack of hemolytic properties upon addition to blood.

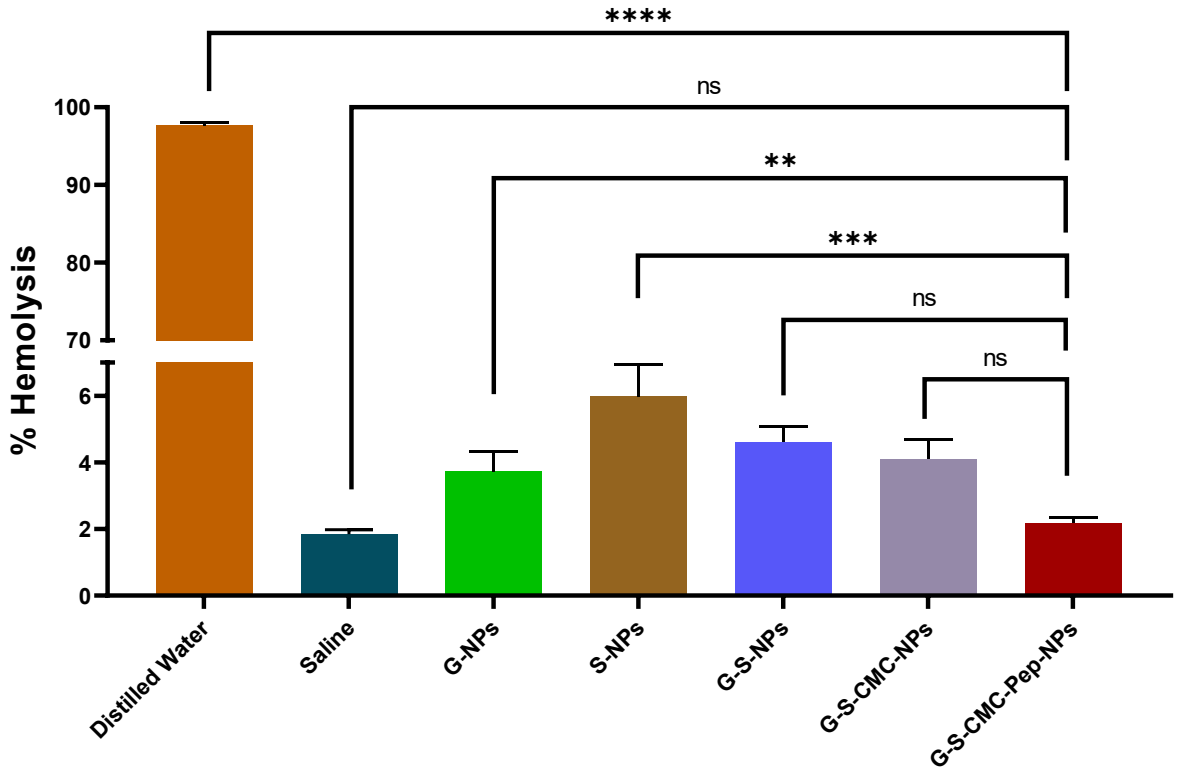

Figure 5.14. Hemolysis of nanoparticles in healthy erythrocytes induced by distilled water, saline, G-NPs, S-NPs, G-S-NPs, G-S-CMC-NPs and G-S-CMC-Pep-NPs

5.3.4. Nanofiber characterization

5.3.4.1 Contact angle measurement

The observed blank nanofibers contact angles were 34.80 ± 1.58° (left), and 34.49 ± 1.13° (right), while angles of contact for G-S-CMC-Pep-NPs-NFs were 64.64 ± 1.67° (left) and 65.92 ± 1.31° (right) (**Figure 5.15.**). The data demonstrated a substantial decrease in the hydrophilicity of the electrospun nanofibers following the incorporation of G-S-CMC-Pep-NPs into the nanofibers.

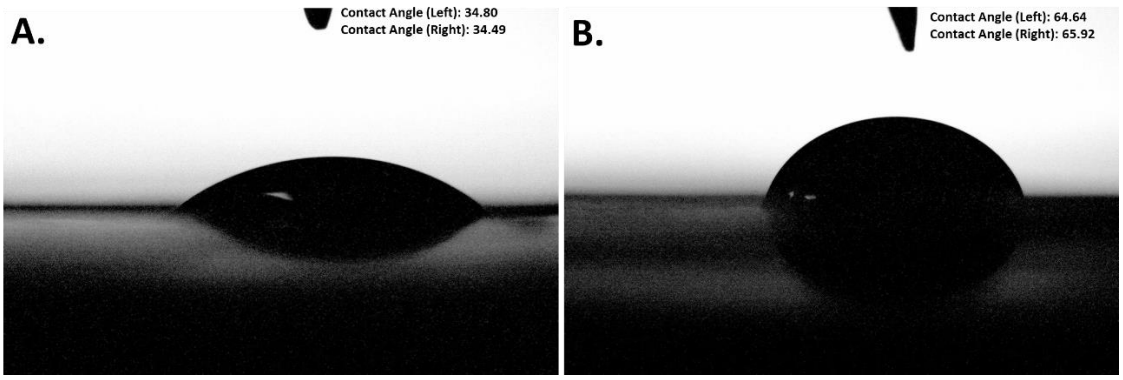

Figure 5.15. Contact angle measurement of A) blank nanofiber and B) G-S-CMC-Pep-NPs-NFs

5.3.4.2. TEM imaging of nanofibers

The TEM images of fibers indicated a distribution of diameter ranging of 100 nm to 400 nm **(Figure 5.16.).** TEM analysis distinctly revealed numerous G-S-CMC-Pep-NPs integrated within the nanofibers, appearing as black dots on their surface, confirming the impact of G-S-CMC-Pep-NPs. In contrast, the blank nanofibers revealed no evidence of nanoparticles incorporated within their matrix. Conversely, G-S-CMC-Pep-NPs-NFs depict nanoparticles of size range from 60 nm to 150 nm. It has been reported that the size of the electrospinning nanofibers usually impacted by different properties of electrospinning, including molecular weight, viscosity, composition of chemical and electrical conductivity of the component polymers [167, 168]. This insight substantiates the presence of G-S-CMC-Pep-NPs within the matrix of nanofibers [169].

5.3.4.3. SEM imaging of nanofibers

SEM imaging reveals a uniform and homogeneous network of cross-linked fibers, exhibiting dimensions ranging of 100 to 500 nm **(Figure 5.17.).** The component displayed a sustained and complex three-dimensional matrix structure defined by interconnected voids in both instances. These results indicated a textured interface morphology, attributed to the integration of nanofibers within the pore walls, which is beneficial for cell adherence.

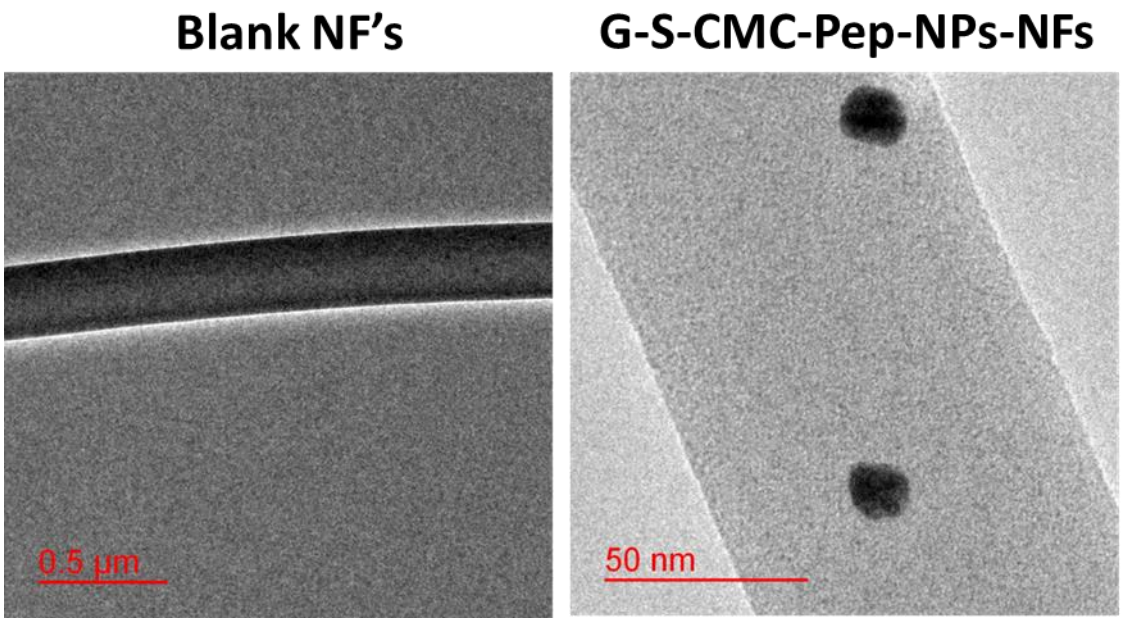

Figure 5.16. TEM analysis of blank nanofiber and G-S-CMC-Pep-NPs-NFs

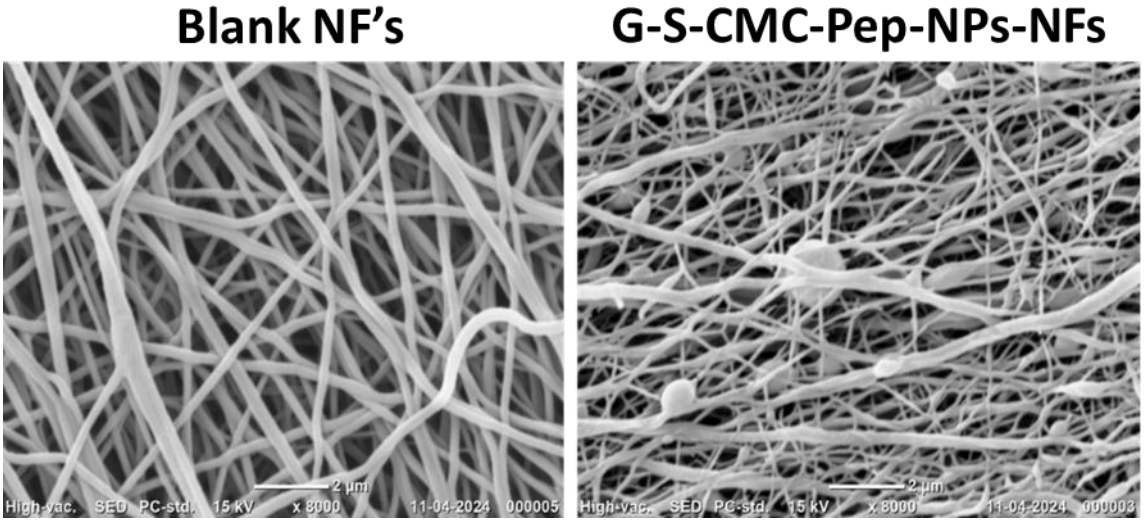

Figure 5.17. SEM analysis of blank nanofiber and G-S-CMC-Pep-NPs-NFs

5.3.4.4. AFM imaging of nanofibers

Two-dimensional phase and three-dimensional height images from AFM were acquired using the intermittent contact approach (**Figure 5.18.**). Samples exhibited remarkable axial alignment within the fiber structures, distinguished by comparatively smooth textures. There was no noticeable assembling observed when G-S-CMC-Pep-NPs were

appropriately incorporated into the nanofibers. Moreover, the analysis revealed no significant differences in rough texture along along the longitudinal or transverse axes, demonstrating an efficient distribution of the roughness traits within the fibers of PVA. The accumulation of particular fibers led to formation of hybrid architectures comprising multiple nanofibers. From the above observations, it can be postulated that the processed fibers facilitated the advancement of interwoven architectures accountable for the formation of homogeneous web of fibers.

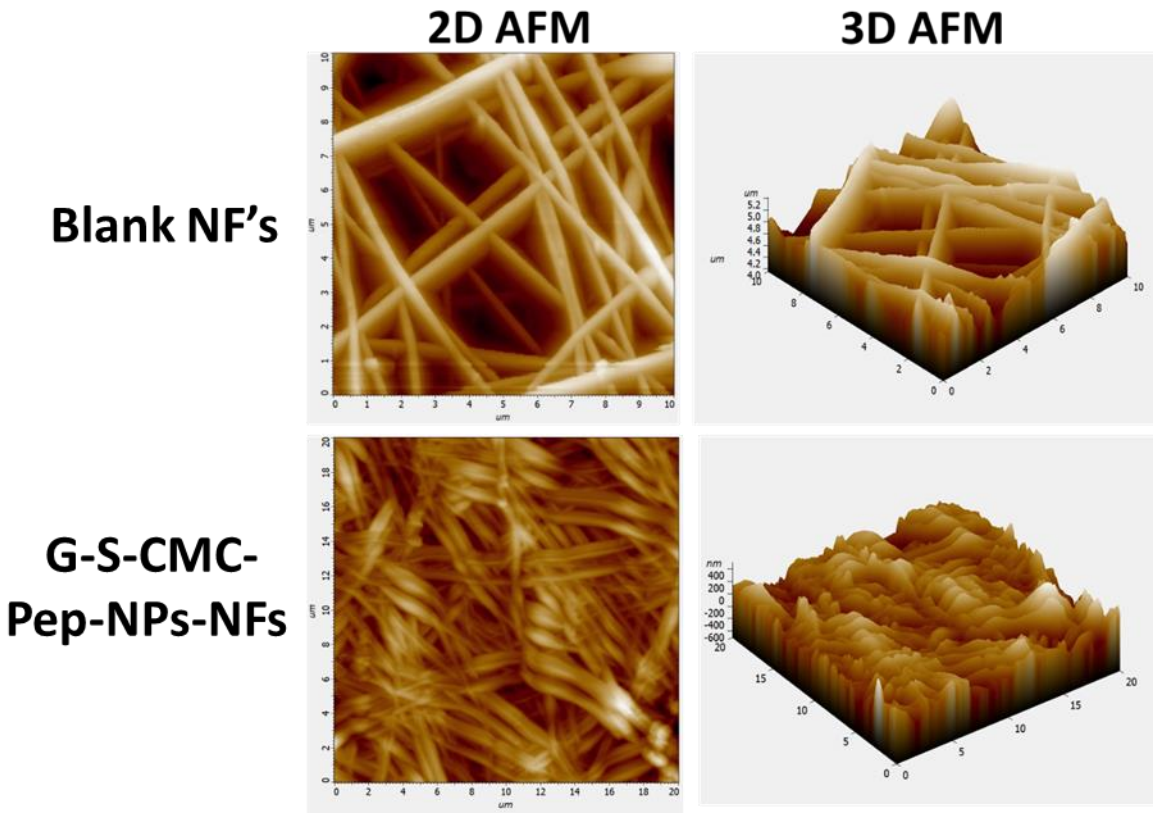

Figure 5.18. AFM analysis of blank nanofiber and G-S-CMC-Pep-NPs-NFs

5.3.4.5. FT-IR investigation

The samples showed wide and well-defined peaks at around 3414 cm^{-1}, which correspond to the O-H and N-H stretching, respectively **(Figure 5.19.)**. Shift of the peaks to lower wavenumbers is ascribed to the increased PVA-chitosan constituents in the samples, signifying the creation of hydrogen bonds formation between PVA-chitosan and CMC

molecules. This shift occurs owing to the presence of free hydroxyl groups in PVA and free amine group in chitosan, indicating potential intermolecular hydrogen bonding between the two polymers. The peptide LL-37 showed the peak shift after functionalization of G-S-CMC-Pep-NPs with the layering of PVA/chitosan. where, the main amide I peak of the peptide is centered at 1598 cm^{-1}, this can be attributed to αhelical and β-sheet structures of the peptide. The -CH_2- rocking band in PVA/chitosan-containing nanofibers was detected at 724 cm^{-1}. The integration of nanoparticles within the blank nanofibers resulted in a significant decrease in the absorbance of the corresponding peaks. The peak of C-O bonds observed at 1100 cm^{-1} found in PVA nanofibers, which is influenced by the crystallization of PVA, resulting in a shoulder-like appearance. The peak at 1260 cm^{-1} arises from the C-O stretching vibrations, while the symmetric bending mode vibrations of PVA's CH-OH and CH_2 groups are reflected in peaks at 1370 cm^{-1} and 1430 cm^{-1}.

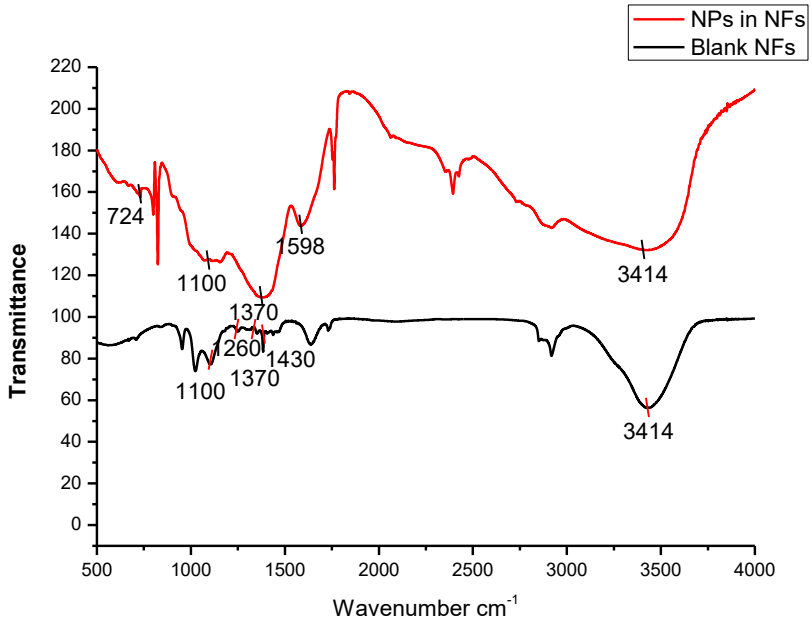

Figure 5.19. FT-IR investigation of blank nanofiber and G-S-CMC-Pep-NPs-NFs

5.3.4.6. XRD of nanofibers

XRD analysis was employed to investigate the crystalline nature of the nanofibers. XRD spectrum of the blank fibers exhibited a broad peak (2θ of 24°), indicative of their non-crystalline structure, while the spectrum for G-S-CMC-Pep-NPs-NFs displayed multiple well-defined peaks (2θ of 11°, 19°, 21°, 22°, 27°, 30° and 33°), signifying a polycrystalline nature **(Figure 5.20.).** This finding suggests that the presence of polycrystallographic orientations within the nanofiber matrix may significantly influence various critical properties pertinent to healing of wound. Specifically, crystal interfaces among the crystal phases may affect the deformation properties of nanofibers, thereby impacting their elasticity and resilience. Such characteristics are vital for confirming that the nanofibers material can effectively respond to the kinetic and complex elastic conditions in wound healing process.

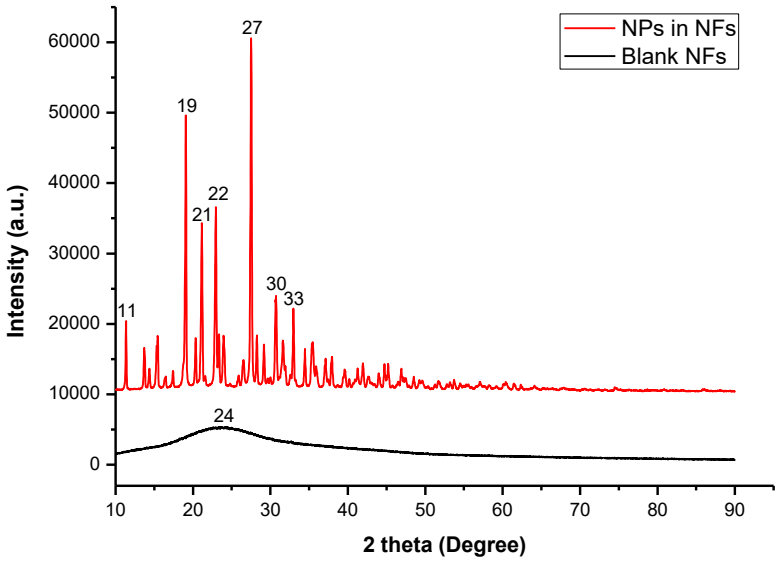

Figure 5.20. XRD investigation of blank nanofiber and G-S-CMC-Pep-NPs-NFs

5.3.4.7. Aspects of nanofiber release

The release kinetics of G-S-CMC-NPs and G-S-CMC-Pep-NPs-NFs exhibited values of 84.56 ± 2.01% and 26.80 ± 3.98%, respectively, after 8 hr **(Figure 5.21.)**. In contrast to G-S-CMC-NPs, which shows a quick and maximum release within 18 hours, G-S-CMC-Pep-NPs-NFs released and distributed the bimetallic complex gradually over 48 hours. Although G-S-CMC-Pep-NPs may be more appropriate for the short-duration administration of medicines, these data suggest that G-S-CMC-Pep-NPs-NFs has the capacity for prolong release.

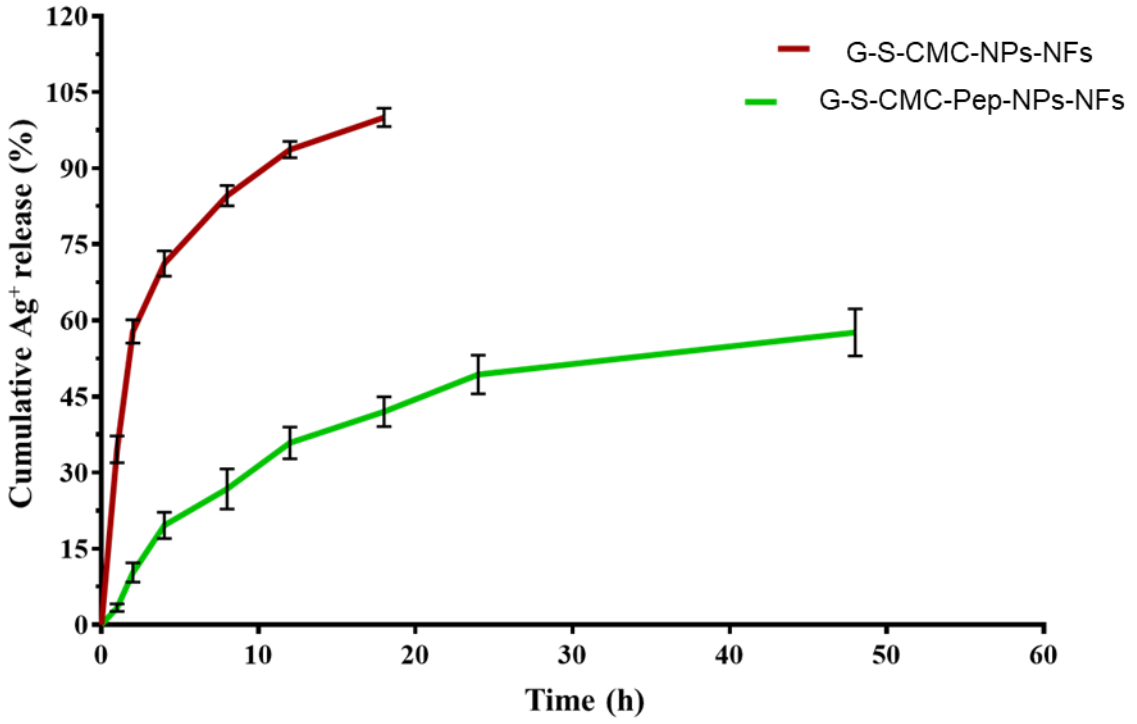

Figure 5.21. *In vitro* release of Ag^{+} ions from nanoparticles and nanofibers

5.3.4.8. Hemolytic investigation of nanofibers

Hemolysis activity elicited by distilled or deionized water, saline, G-S-CMC-Pep-NPs and G-S-CMC-Pep-NPs-NFs were 98.11 ± 1.13%, 1.56 ± 0.16%, 2.18 ± 0.16% and 1.42 ± 0.09%, signifying that nanofibers exhibited non-hemolytic characteristics. This

substantiates that the nanofibers can be regarded as non-hemolytic composition **(Figure 5.22.)**.

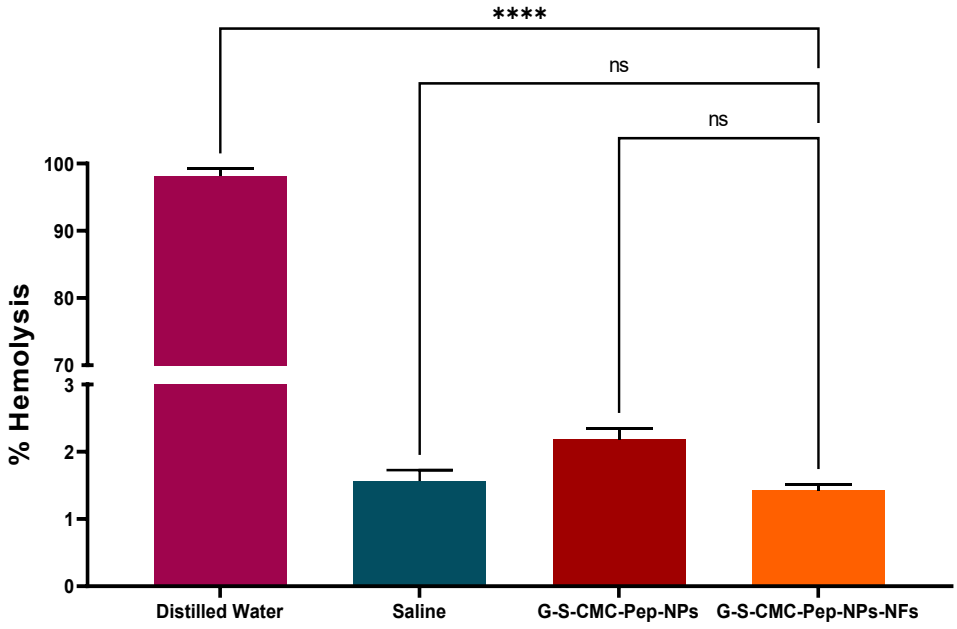

Figure 5.22. Hemolysis in healthy erythrocytes induced by distilled water, saline, G-S-CMC-NPs and G-S-CMC-Pep-NPs-NFs

5.3.4.9. pH of nanofibers

pH measurements of blank nanofiber dressing and G-S-CMC-Pep-NPs-NFs dressing were 6.86 ± 0.61 and 5.43 ± 0.19 **(Figure 5.23.)**. Nanofibers matrix was engineered to create a slightly acidic microenvironment conducive to the regulation and inhibition of bacterial growth and infection progression. This design is predicated on the observation that numerous pathogenic bacteria thrive in neutral or slightly alkaline pH ranges. Furthermore, maintaining a mildly acidic pH may enhance specific components of tissue regeneration, including the activity of enzymes that play crucial roles in tissue regeneration [170]. Consequently, it can be inferred that acidic impact of G-S-CMC-Pep-NPs-NFs films provide a suitable environment conducive to enhancing tissue proliferation and promoting connective tissue cell growth.

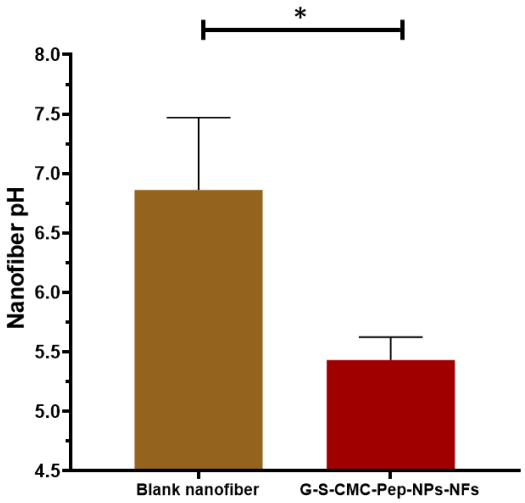

Figure 5.23. pH of nanofibers. Statistical significance among groups was calculated by t-test, (n= 3; the value * ($p < 0.05$), was considered for significance level determination)

5.3.4.10. Competence in blood clotting

G-S-CMC-Pep-NPs-NFs exhibited a markedly reduced absorbance compared to both the blank nanofiber film and pure blood, indicating its superior blood clotting efficacy **(Figure 5.24.).** The inclusion of bimetallic nanoformulations notably enhanced the blood clotting capacity of the nanofibers.

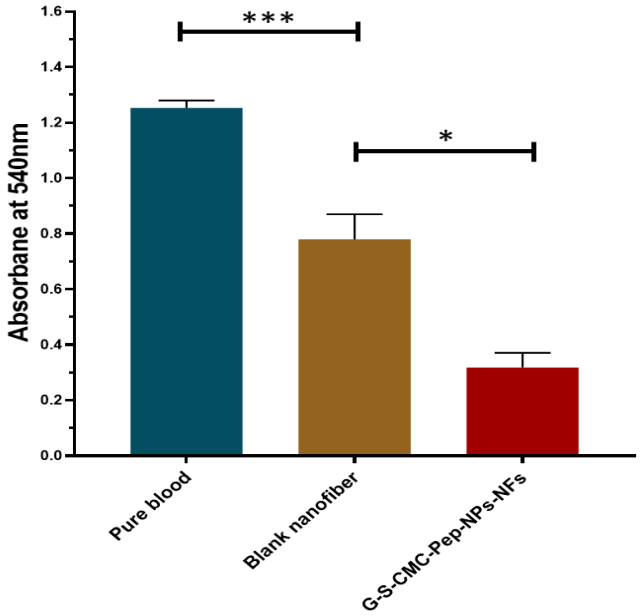

Figure 5.24. The assessment of the coagulation capacity of whole blood. Statistical significance among groups was calculated by t-test, (n= 3; the values ns ($p \geq 0.05$), * ($p < 0.05$), ** ($p < 0.01$), *** ($p < 0.001$), and **** ($p < 0.0001$) were considered for significance level determination)

5.3.4.11. Thrombus formation study

In comparison to the blank nanofiber, formation of clot was markedly increased when blood sample was treated with the G-S-CMC-Pep-NPs-NFs **(Figure 5.25.).** The hemostatic results demonstrated that G-S-CMC-Pep-NPs-NFs exhibited superior capabilities in promoting fibrin formation and vascular occlusion, making it the optimal choice for enhancing hemostatic efficacy.

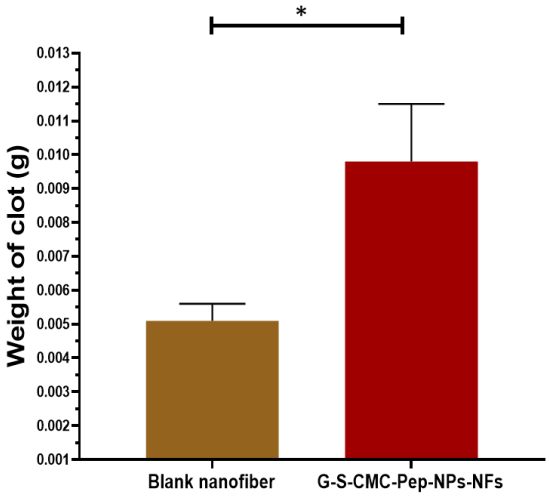

Figure 5.25. Thrombus development of blank and G-S-CMC-NPs-NFs films. Statistical significance among groups was calculated by t-test, (n= 3; the value * ($p < 0.05$), was considered for significance level determination)

5.3.4.12. Water retention ability

Blank nanofibers demonstrated a weight/mass increase of 801 ± 59% relative to their initial mass after immersion in PBS solution for 48 hours. In comparison, nanofibers containing

nanoparticles exhibited a weight gain of 1309 ± 83% from their original mass under the same conditions. Therefore, it can be confirmed that G-S-CMC-Pep-NPs-NFs exhibit superior aqueous retention properties compared to other formulations. The inherent ability of these nanofibers to uptake and retain water underscores their significance in wound healing applications, where moisture management is critical for optimal healing outcomes.

5.3.4.13. Characteristics of nanofiber stability and degradation

Nanofiber stability and degradation were evaluated after thirteen days of regular immersion in PBS solution. The electrospinning nanofibers demonstrated remarkable stability, exhibiting no significant degradation during this period. Samples remained intact and could be effectively grasped with forceps even after 10 days of sustained immersion in water. To simulate *in vivo* conditions, an *in vitro* degradation experiment was conducted, taking into account the existence of lysozyme in various body liquids or fluids, such as serum and tears [171]. Additionally, we assessed the percentage rate of weight-loss of both types of nanofibers was assessed. Specifically, the blank nanofibers exhibited a weight loss of 45.78 ± 4.89%, while the G-S-CMC-Pep-NPs-NFs demonstrated a markedly reduced weight loss of 16.36 ± 2.80%. This indicates the nanofibers' biological resilience, ensuring their biocompatibility with living cells and tissue while minimizing the risk of adverse reactions or degradation.

5.3.5. USM nanoclusters

Fluorescence spectra of the synthesized USM were obtained using a spectrofluorophotometer. The USM dispersion in deionized water was analyzed for fluorescence intensity, and corresponding pictures were taken. As illustrated in **Figure 5.26. A**, USM exhibited blue fluorescence under 366 nm excitation and green fluorescence under 469 nm excitation. USM exhibited fluorescence in IVIS at excitation 469 nm **(Figure 5.26.**

B). TEM images have confirmed the ultra-small and homogeneous size of the USM **(Figure 5.26. C)**. Furthermore, the liquid suspension of USM displayed excitation spectra at 366 nm and 469 nm, with emission peaks at 451 and 543 nm **(Figure 5.26. D)**. Therefore, the developed USM shows reliable potential as promising fluorescent agent for both *in vitro* and *in vivo* applications.

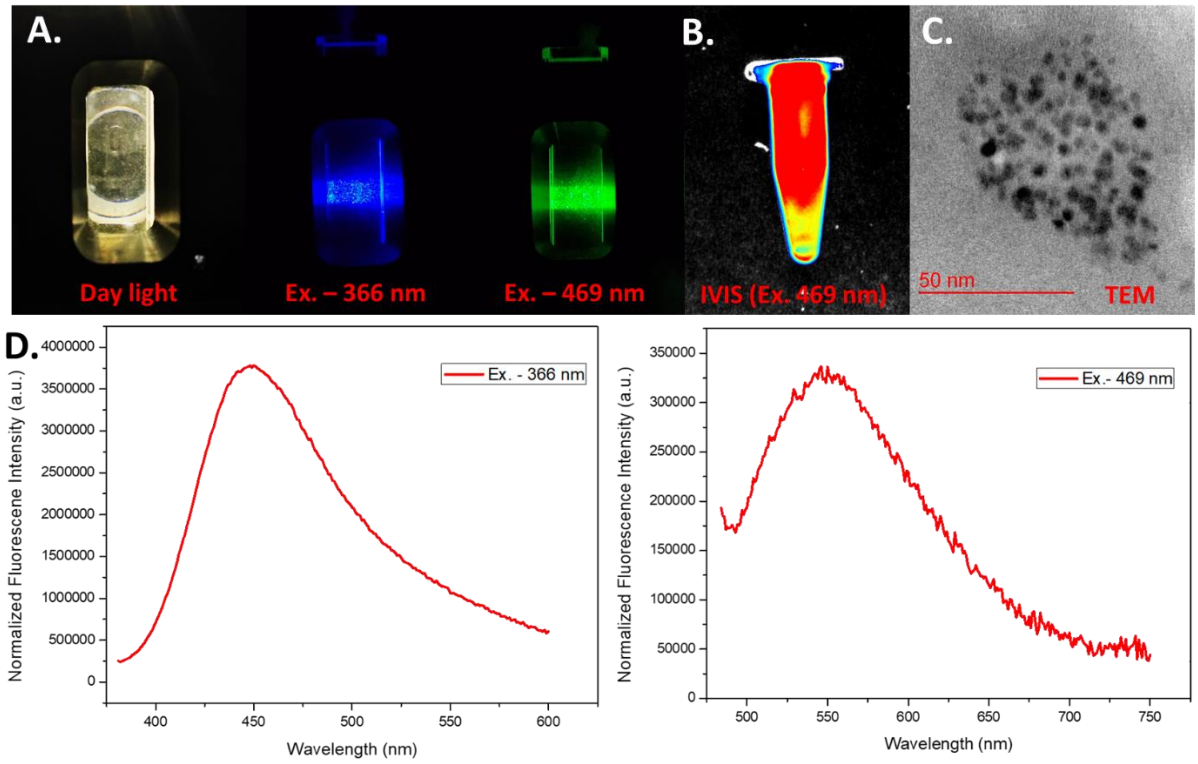

Figure 5.26. A) Fluorescent imaging of USM was performed under daylight conditions, as well as with excitation at 366 nm (blue fluorescence) and 469 nm (green fluorescence) B) IVIS imaging of USM at 469 nm excitation, C) TEM imaging of USM and D) Excitation spectra of USM.

5.3.6. Wound healing investigation

Investigation of G-S-CMC-Pep-NPs-NFs was systematically evaluated at distinct intervals, specifically on days 1, 4, 8, and 12 at the site of wound. It was noted that the wounds in the untreated control group exhibited no significant healing progression throughout the study

period **(Figure 5.27.)**. The order of the wound healing efficacy is as follows: G-S-CMC-Pep-NPs-NFs significantly enhanced wound healing progress in the group inoculated with MDR isolated *P. aeruginosa*, afterwards the non-infected group administered with G-S-CMC-Pep-NPs-NFs, the uninfected group administered with the commercially available antibiotic, and the MDR isolated *S. aureus*-infected group administered with G-S-CMC-Pep-NPs-NFs, while the untreated wounds remained unhealed. Additionally, this investigation is substantiated through comprehensive histopathological analysis of the wound tissue **(Figure 5.28.).** Wounds inocculated with MDR isolated *P. aeruginosa* that were administered with G-S-CMC-Pep-NPs-NFs had the highest wound healing rate, at 92.49% **(Figure 5.27.).** This demonstrates the combination of G-S-CMC-Pep-NPs-NFs exhibited superior efficacy on MDR *P. aeruginosa*-infected wounds compared to other treatment groups. Wound healing trajectory varies significantly upon infection with different bacteria, as chronic wounds are triggered by the persistent colonization of particular bacteria within the tissue microenvironment. Release of bacterial endotoxins drives prolonged elevation of interleukin-1, pro-inflammatory cytokines and tumor necrosis factor α. This persistent inflammatory state results in increased matrix metalloprotease activity, a concomitant decrease in tissue inhibitors, and impaired growth factor synthesis. Although inflammation is an intrinsic phase of wound healing process, an exaggerated inflammatory reaction can impede tissue regeneration. Bacteria are pivotal in modulating a controlled inflammatory response necessary for effective wound healing. Subinfective bacterial loads have been shown to enhance wound repair and granulation tissue formation, characterized by increased recruitment of monocytes, macrophages, neutrophils, and elevated prostaglandin E-2 expressions, and enhanced collagen synthesis.

Moreover, several studies have documented incorporation of metallic nanoformulations within the matrix polymeric framework of CMC that exerted a

pronounced antibacterial effect, significantly impeding bacterial proliferation [158] whereas, LL37 demonstrated bacteriostatic properties characterized by direct suppression of bacterial proliferation and attenuation of MDR *P. aeruginosa*-induced cytokine secretion [172]. The antimicrobial activity of metallic nanoformulations and the associated release of ions is majorly attributed to the disintegration of biofilm architecture and disruption of its cell wall membrane components, along with the suppression of bacterial metabolic pathways through multiple mechanisms. These G-S-CMC-Pep-NPs-NFs nanofibrous constructs, likely serving as scaffolds or wound dressings, exhibit potent antibacterial properties, particularly against MDR bacterial strains that developed resistance to conventional therapeutics. The incorporation of LL-37, CMC, and silver nanoformulation within the nanofiber-matrix prominently enhances its antibacterial efficacy, presenting substantial potential for advanced wound care applications. Furthermore, this strategy demonstrates a novel approach to promoting wound healing, especially in MDR-microbe infected wounds without eliciting adverse effects.

5.3.7. Western blotting analysis

Re-epithelialization of the wound necessitates the proliferation and migration of surrounding keratinocytes across the wound. The keratinocytes underwent EMT to achieve scar formation and healing of the wound. The mesenchymal marker Vimentin gets upregulated during EMT [173]. To investigate the expression of Vimentin in healing of wound after exposure to prepared G-S-CMC-Pep-NPs-NFs, were prepared protein lysate from the wound tissues of infected mice with MDR *P. aeruginosa* and MDR *S. aureus*, therapy with the formulation G-S-CMC-Pep-NPs-NFs. Protein samples from uninfected and no treatment mice and treatment with commercially available formulation were also collected and used as the controls.

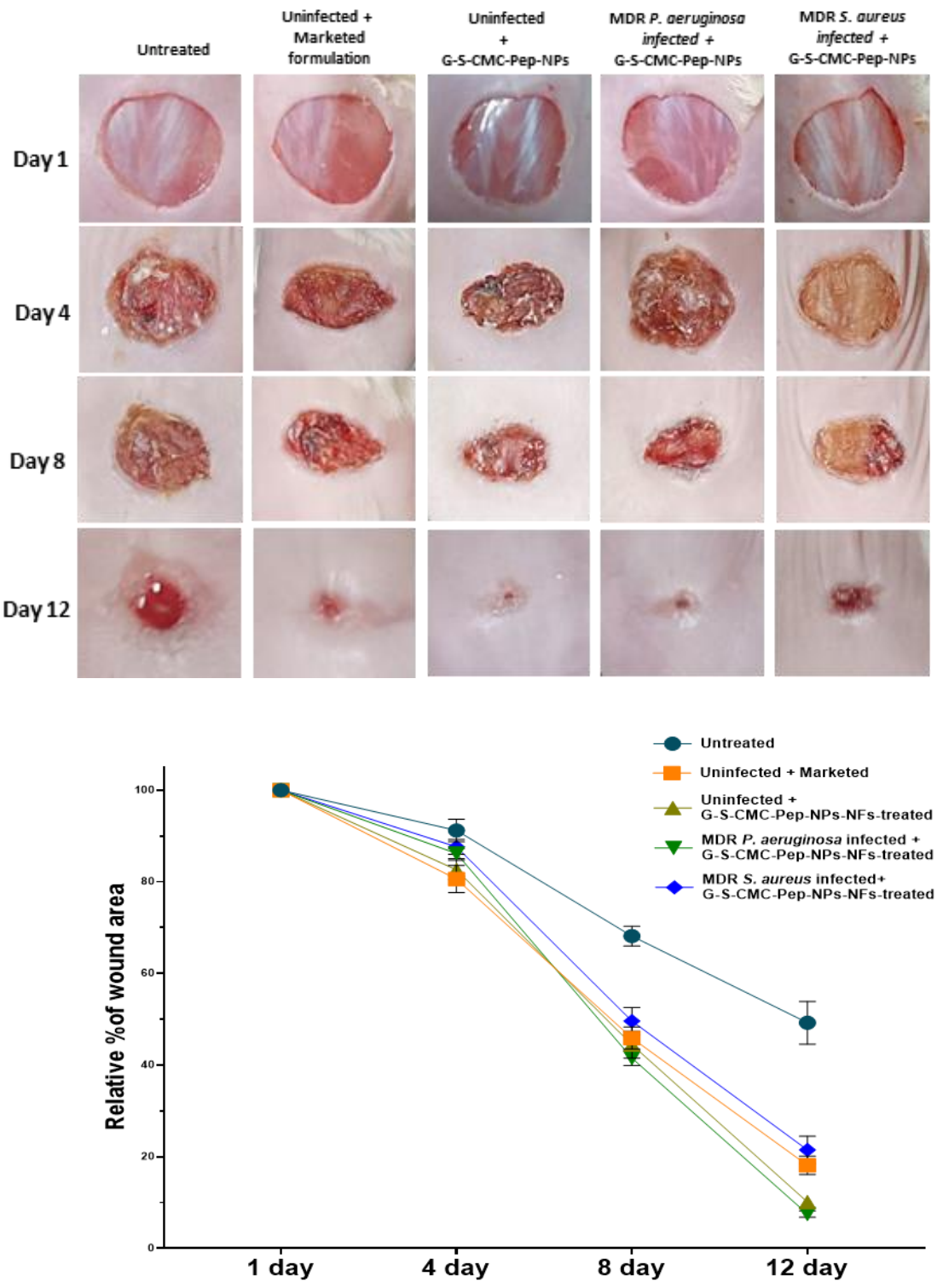

Figure 5.27. Wound healing investigation images- wound size reduction in murine models and the relative proportion of wound area is graphically shown across mice treatment groups on days 4, 8, and 12.

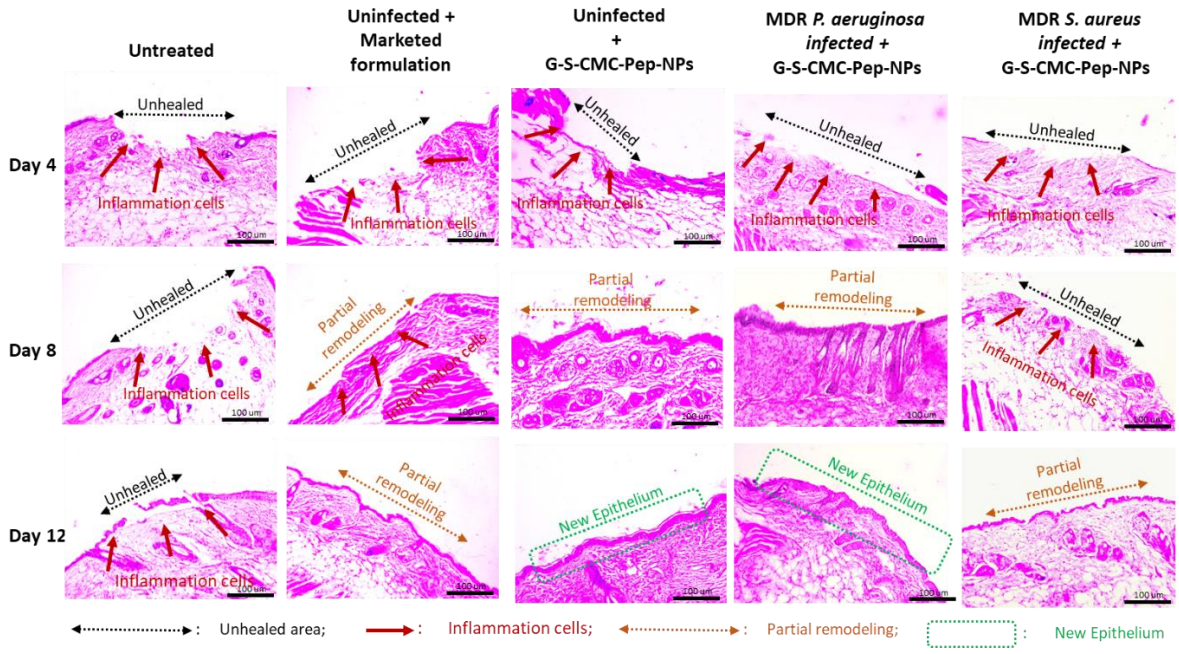

Figure 5.28. Histological analysis of skin tissue was conducted using a brightfield microscope at 100× magnification on days 4, 8, and 12

Signaling pathway known to mediate the upregulation of Vimentin facilitating EMT. is EGFR/ERK signaling [154]. Activation of EGFR upon binding with its ligands leads to the phosphorylation of ERK-1/2 resulting in subsequent initiation of the genes involved in EMT [174]. Wound healing assessment and H&E staining results indicated no significant difference between the untreated pathogen-infected groups and the controls. Key groups were selectively analyzed with significant outcomes for protein expression. To check the activation of EGFR/ERK signaling in wound healing upon treatment with G-S-CMC-Pep-NPs, we examined the expression of EGFR receptor and phosphorylation status of ERK-1/2 via western blotting in samples from uninfected mice that were untreated and treated with marketed formulation and infection with MDR *P. aeruginosa* and *S. aureus* that exposed to G-S-CMC-Pep-NPs-NFs. Both EGFR receptor levels and the phosphorylation of ERK 1/2 were found to be increased in G-S-CMC-Pep-NPs treated wounds from *P. aeruginosa* infected mice compared to the controls. Treatment of the wounds with NPs in

S. aureus infected mice showed only mild increase in the levels of EGFR and p-ERK-1/2 compared to the untreated and market formulation-treated controls **(Figure 5.29.).** Quantification of the protein band intensities of EGFR and p-ERK 1/2 suggested a significant acceleration in wound healing was noted in G-S-CMC-Pep-NPs treated wounds of *P. aeruginosa* mice and a milder rate of wound healing in *S. aureus* infected mice compared to the controls. Our studies suggested that treatment with G-S-CMC-Pep-NPs-NFs improves and accelerates healing in the mice via activation of EGFR-ERK signaling leading to activation of the genes that contribute significantly to healing of the wound **(Figure 5.29.).**

Figure 5.29. illustrates the band intensities of Vimentin, EGFR, and p-ERK-1/2 in mice subjected to wounds and infected with microbes, which were exposed with nanofibers containing therapeutic nanoparticles. The control groups consisted of the mice that did not receive any therapy and those who received the commercially available formulation. Notably, the levels of these markers were consistently increased in mice inocculated with MDR isolated *P. aeruginosa* and exposure with G-S-CMC-Pep-NPs-NFs. In contrast, a modest increase in the expression of these markers was observed in mice infected with MDR isolated *S. aureus* that received treatment with our formulation.

Western blotting indicated the molecular mechanism by which G-S-CMC-Pep-NPs–NFs lead to accelerated healing of wound in mice. Exposure with G-S-CMC-Pep-NPs-NFs formulated in our lab led to the activation of EGFR/ERK signaling as evidenced by the increased band intensity of EGFR receptor and phosphorylation of ERK-1/2 in the protein samples obtained from wound tissues of *P. aeruginosa* infected mice compared to the controls. Treatments including hydrogels leading to the activation of EGFR have been found to enhance wound healing in various model systems including human tissue samples by promoting EMT and proliferation. Also, downregulating EGFR in tumorigenic

conditions has shown suppression of proliferation. Thus suggesting the paramount role of EGFR in wound healing via inducing the activation of genes leading to proliferation [175]. Vimentin, the mesenchymal marker implicated in EMT is activated by EGFR/ERK signaling. Studies by Walker and the group has proved that upon injury, Vimentin's released in the extra-cellular area and adheres to the membrane of mesenchymal stem cells located at the periphery of the wound within the native extracellular matrix milieu and facilitates its closure [176]. Our studies also exhibited a marked upregulation of Vimentin expressions in G-S-CMC-Pep-NPs-NFs treated wounds of mice infected with *P.aeruginosa* in comparison with the controls. Taken together, the western blotting analysis suggested the involvement of EGFR/ERK signaling in wound healing by inducing the activation of Vimentin upon exposure with G-S-CMC-Pep-NPs-NFs. This highlighted the efficacy and effectiveness of our formulation in healing of the wounds.

5.3.8. Release profile of nanoformulation via IVIS

IVIS analysis enabled an indirect quantitative assessment of nanoparticle bio-distribution dynamics over a defined temporal period **(Figure 5.30.)**. In this study, the liberation of free USM from the control blank nanofibers and G-S-CMC-Pep-NPs-NFs-USM following exposure to various microbial pathogens 48h post-exposure. Release profile was assessed at specific time points: 10 minutes, 1 h, 2 h, 4 h, 8 h, 24 h, and 48h post-exposure. The fluorescence intensity of the USM was quantified as radiant efficiency (photons/sec/cm²/sr). It was observed that USM was released rapidly from the blank nanofibers, with detectable free USM appearing 4 h post-application, followed by a prominent decline in signals of fluorescence, ultimately vanishing entirely by 48 hours. In contrast, the USM-loaded nanofibers containing USM loaded nanofibers (G-S-CMC-Pep-NPs-NFs-USM) demonstrated a sustained and controlled release profile, characterized by a gradual reduction in fluorescent intensity. This indicates that the nanoparticles can

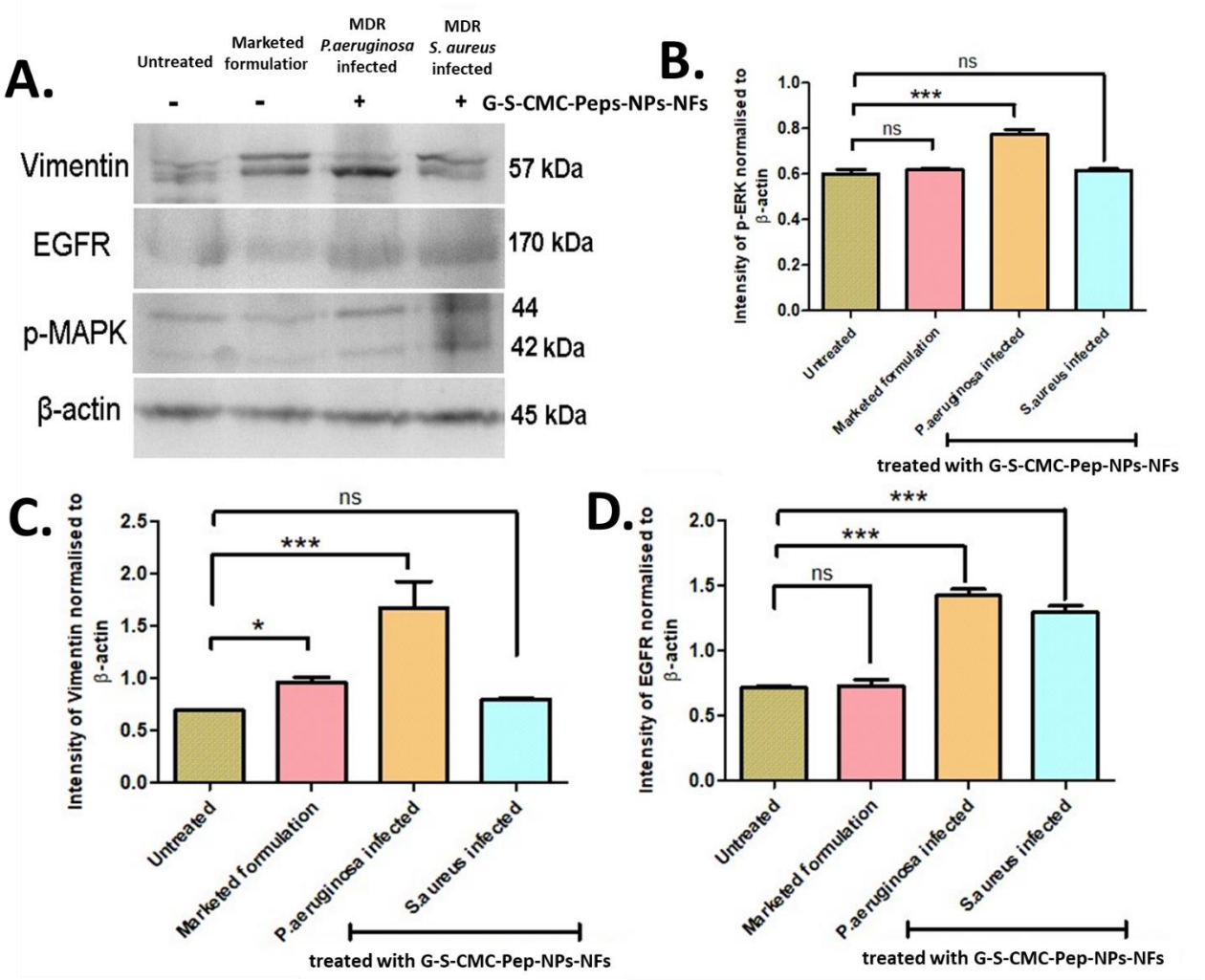

Figure 5.29. Western blotting analysis **(**A) G-S-CMC-Pep-NPs-NFs promoted wound healing in animals; (B) Relative % of p-ERK wound marker expressions; (C) Relative % of Vimentin wound marker expressions; (D) Relative % of EGFR wound marker expressions

provide a prolonged therapeutic presence at wound sites, ensuring effective treatment over an extended duration. These findings validate the sustained and controlled delivery of nanomaterials from nanofibers to wound environments, resulting in a beneficial therapeutic outcome.

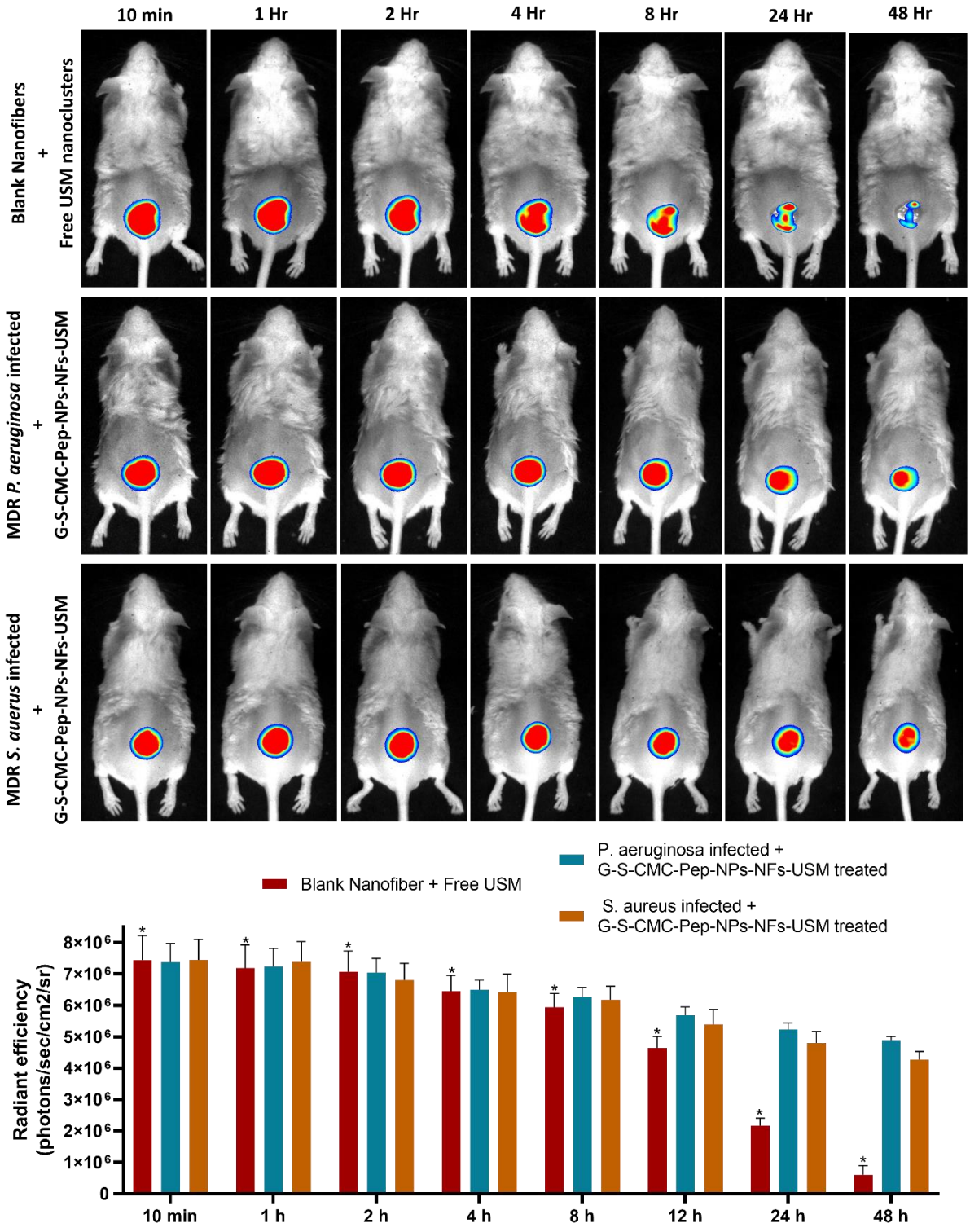

Figure 5.30. *In vivo* real-time optical imaging was employed to assess the biodistribution of free USM from control blank nanofibers and G-S-CMC-Pep-NPs-NFs-USM in the presence of various microbial infections. The distribution was monitored at multiple time points-10 minutes, 1, 2, 4, 8, 24, and 48 hours—following treatment over a 48-hour period.

5.3.9. Live ultrasound/photoacoustic investigation

Photoacoustic investigation of MDR bacterial infected wounds in animals were conducted on day-1 and subsequently at 4^{th}, 8^{th}, and 12^{th} days post-exposure **Figure 5.31. - Figure 5.35.)**. Ultrasound and photoacoustic imaging revealed a significant enhancement in infected wound healing process afterwards the application of nanofiber. Additionally, photoacoustic approach was employed to evaluate the observed variations % sO_2 **(Figure 5.36.)**. The sO_2 % variation on day 12 in wound healing were 56.73 ± 3.13, 73.89 ± 0.85, 88.15 ± 2.95, 82.10 ± 3.55, and 60.65 ± 3.89 for untreated, uninfected-marketed, uninfected + G-S-CMC-Pep-NPs-NFs therapy, mice inoculated with MDR isolated *P.aeruginosa* + G-S-CMC-Pep-NPs-NFs therapy, and mice inoculated with MDR isolated *S. aureus* infected+ G-S-CMC-Pep-NPs-NFs therapy groups.

Percentage rate of vascularity **(Figure 5.36.)** alterations on day 12 in wound healing were 51.46 ± 3.81, 88.46 ± 2.91, 96.63 ± 3.16, 92.13 ± 1.06, and 60.48 ± 4.93 for untreated, uninfected-marketed, uninfected + G-S-CMC-Pep-NPs-NFs therapy, mice inoculated with MDR isolated *P.aeruginosa* + G-S-CMC-Pep-NPs-NFs therapy, and mice inoculated with MDR isolated *S. aureus* + G-S-CMC-Pep-NPs-NFs therapy. The images presented represent peak projection of signal intensities of the healing process captured through 3D-power doppler imaging. These visuals provide a descriptive assessment of vascular flow intensity recorded on day 1^{st}, 4^{th}, 8^{th}, and, 12^{th} day post-exposure. The vascular-index was utilized to statistically evaluate the comparative changes in wound perfusion.

The results from the *in vivo* photoacoustic/ultrasound approach demonstrate the wound healing rate is markedly accelerated in MDR isolated *P. aeruginosa* following treatment with G-S-CMC-Pep-NPs-NFs relative to non-infected wounds and those infected with *MDR S. aureus*. Furthermore, the healing percentage rate in uninfected wounds subjected to G-S-CMC-Pep-NPs-NFs is superior to that of with marketed formulation. In contrast,

the slowest healing rates were evident in non-treated wound. The chronicity of wounds is attributed to the consistency of specific tissue-resident microbes, indicating that the healing process is influenced by the type of microbial infection present.

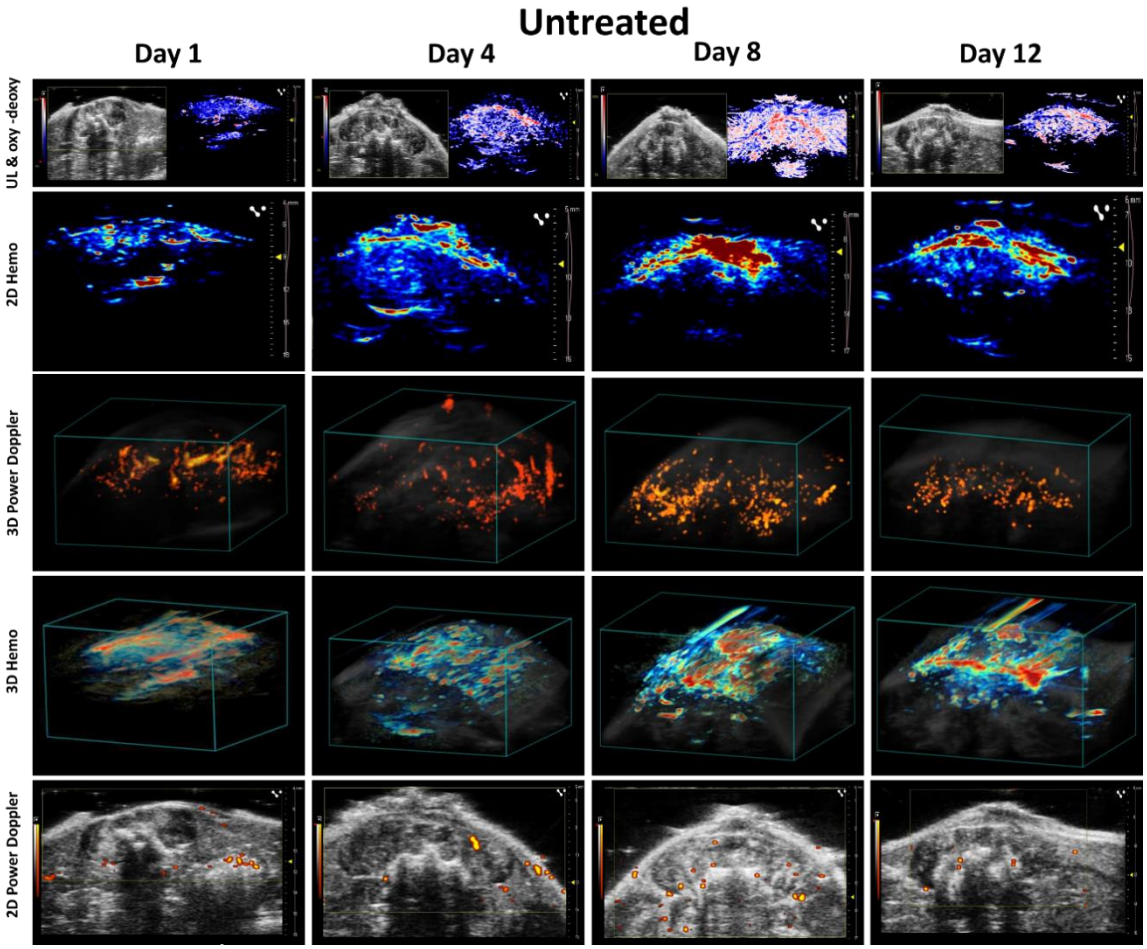

Figure 5.31. Ultrasound/photoacoustic imaging, power Doppler analysis, and oxy-deoxy visualization of the untreated group

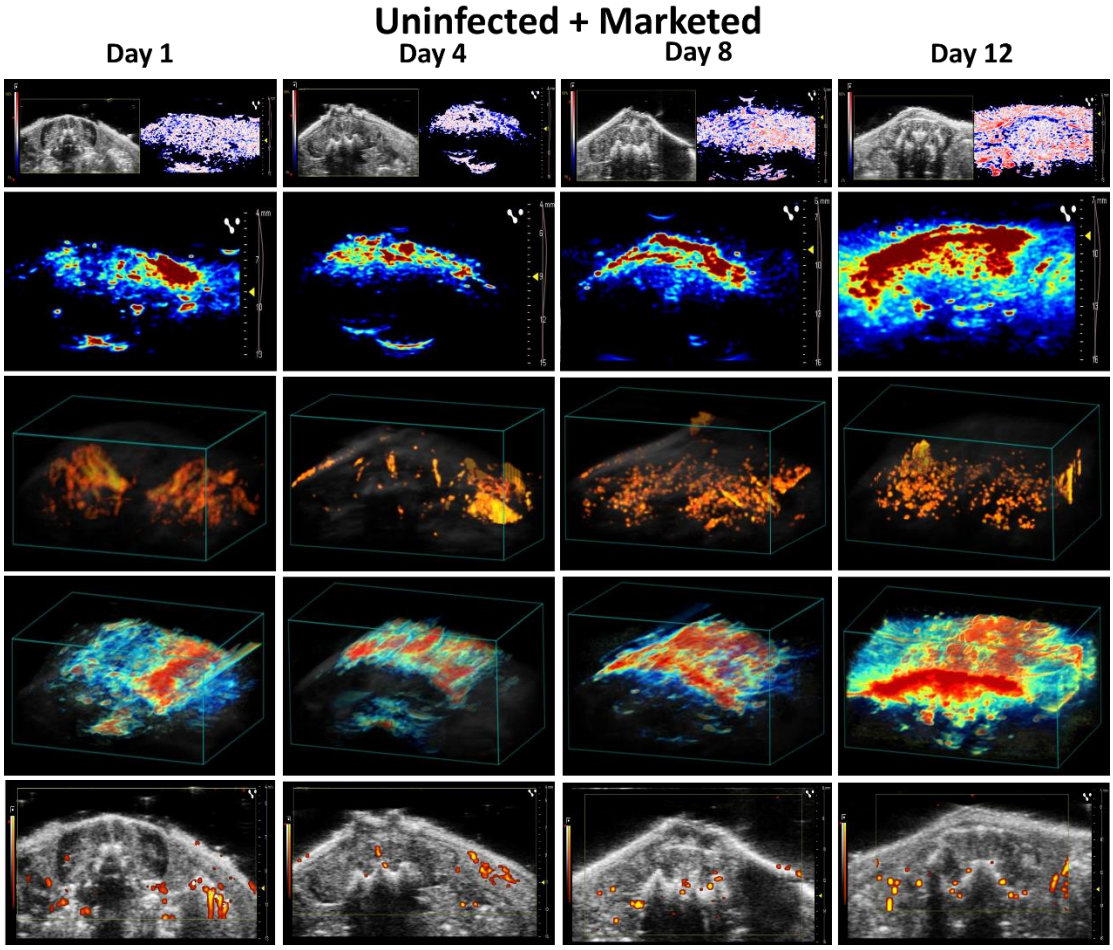

Figure 5.32. Ultrasound/photoacoustic imaging, power Doppler analysis, and oxy-deoxy visualization of the uninfected and marketed treatment group

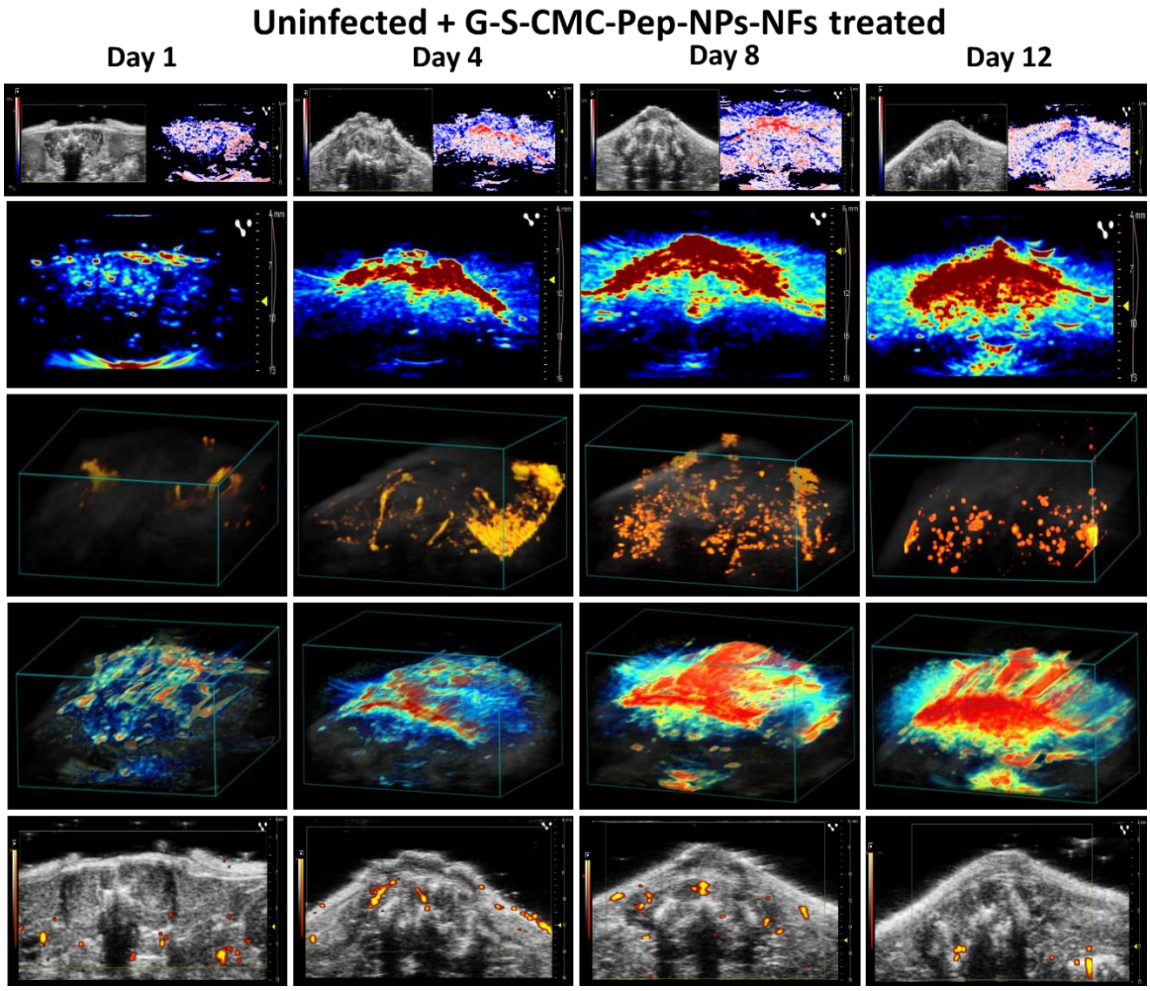

Figure 5.33. Ultrasound/photoacoustic imaging, power Doppler analysis, and oxy-deoxy visualization of the uninfected and G-S-CMC-Pep-NPs-NFs treatment group

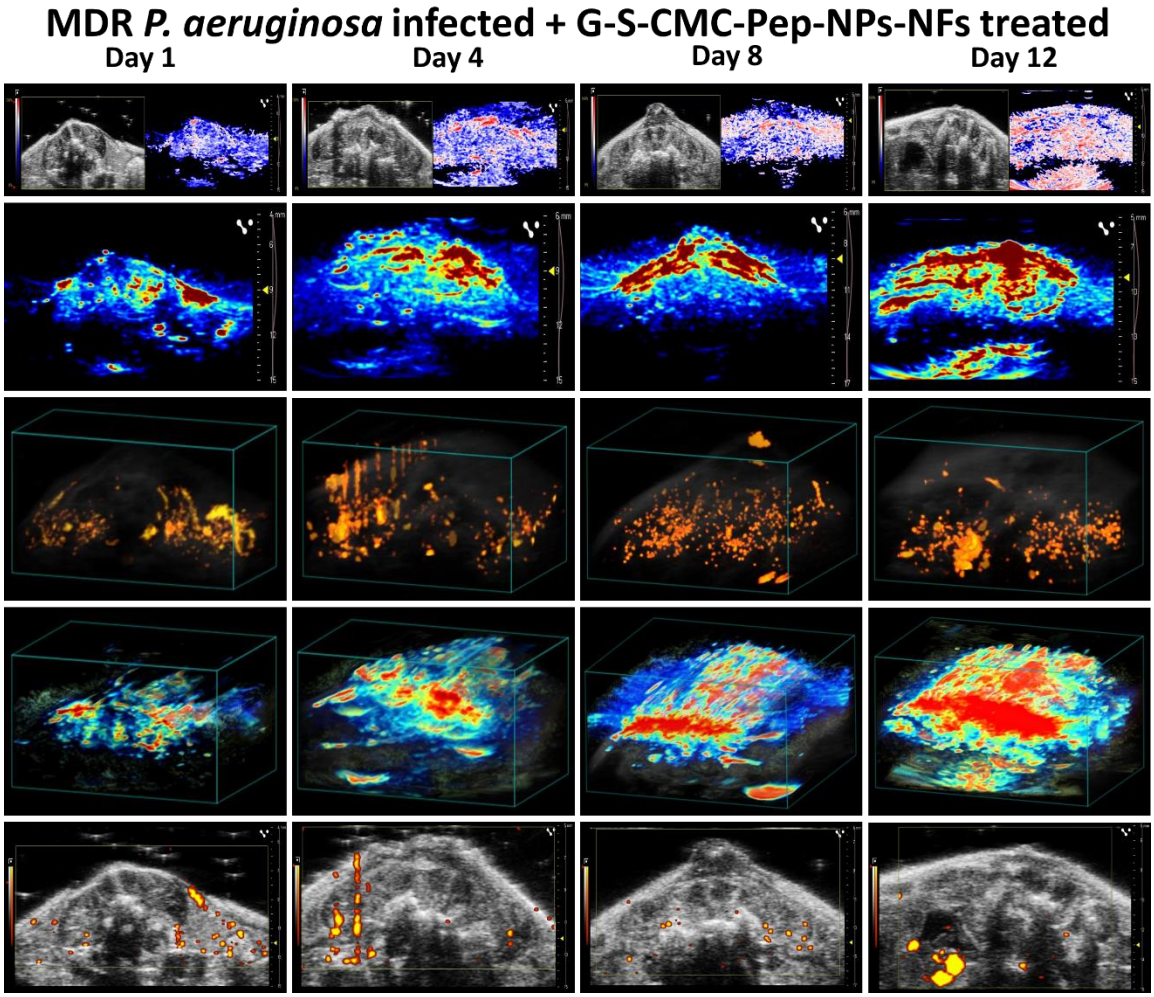

Figure 5.34. Ultrasound/photoacoustic imaging, power Doppler analysis, and oxy-deoxy visualization of the MDR *P. aeruginosa* and G-S-CMC-Pep-NPs-NFs treatment group

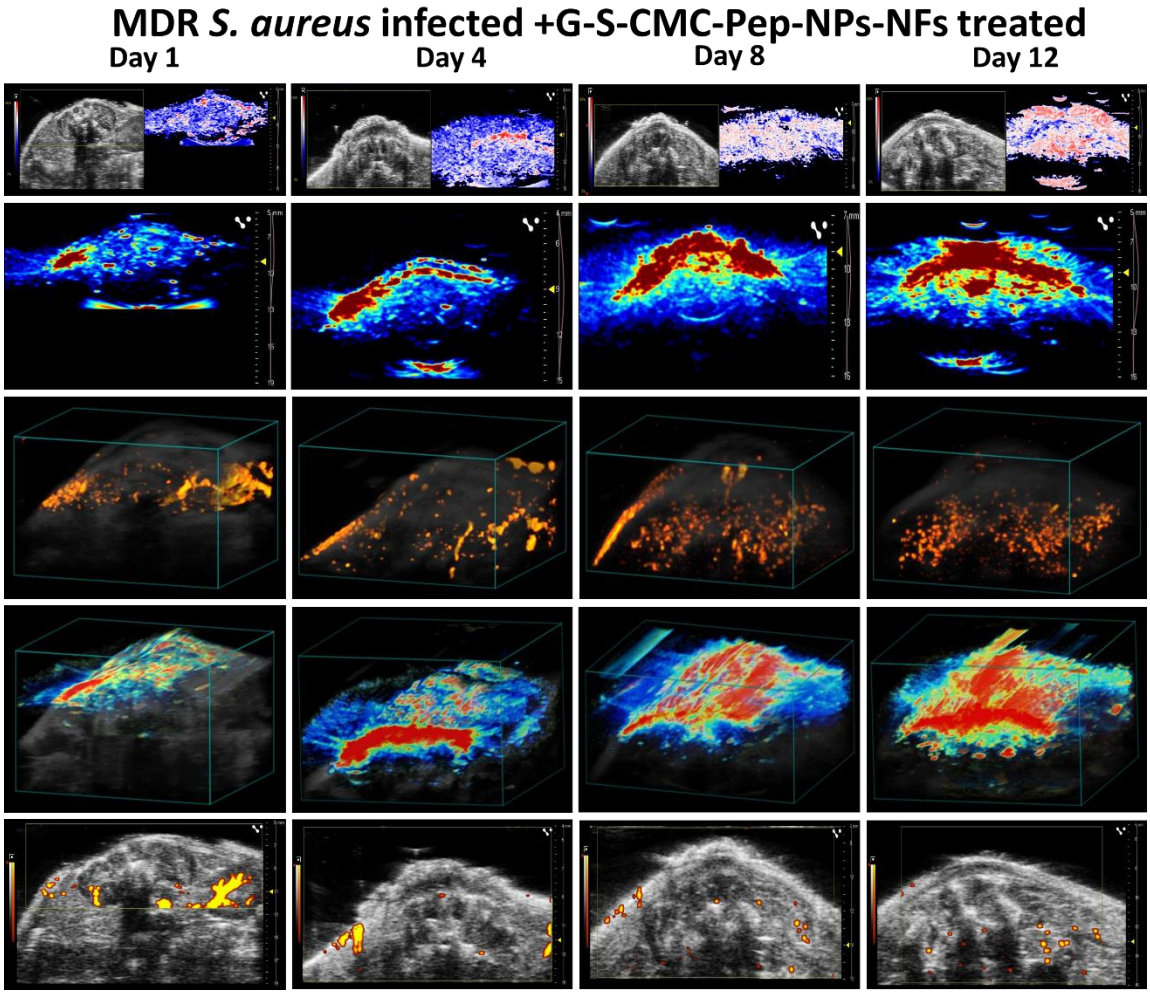

Figure 5.35. Ultrasound/photoacoustic imaging, power Doppler analysis, and oxy-deoxy visualization of the MDR *S. aureus* and G-S-CMC-Pep-NPs-NFs treatment group

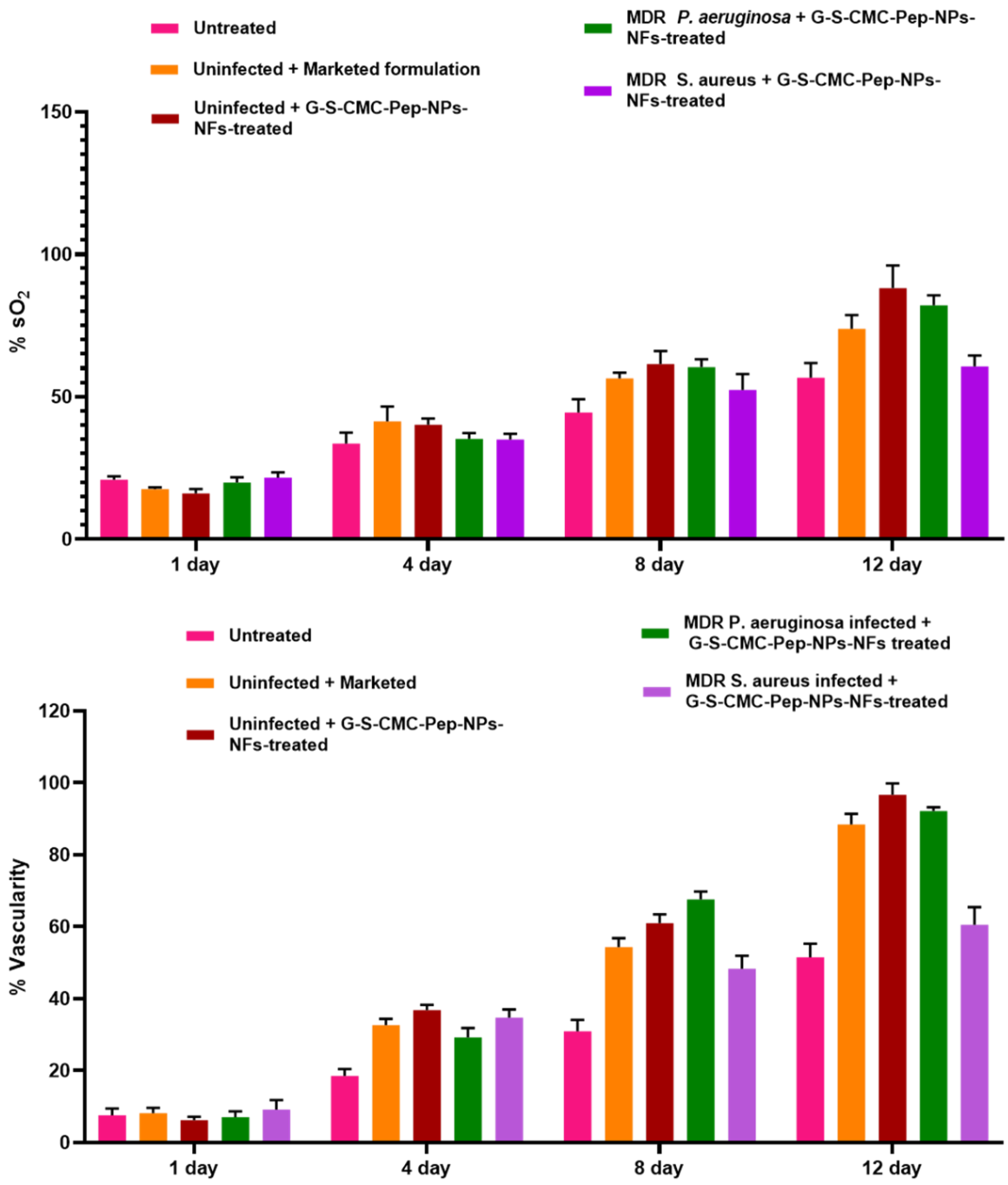

Figure 5.36. Percentage of sO2 in the wounds of the corresponding groups and vascularity percentage of the wounds across the respective groups

5.3.10. Conclusion

This research underscores the remarkable adaptability and therapeutic promise of the LL-37 peptide when synergistically combined with CMC and bimetallic nanoparticles, positioning this composite as a highly effective agent for the accelerated healing of wounds infected with MDR microbes. Unlike many commercial wound care formulations, which are often limited by adverse side effects and suboptimal efficacy against resistant pathogens, the novel dressing designated as G-S-CMC-Pep-NPs demonstrated a sustained and controlled release of its active components directly at the wound site. This localized and prolonged delivery was instrumental in significantly promoting wound closure within a notably short 12-day period. Molecular investigations, particularly western blot analyses, further revealed that application of the nanofiber-based dressing led to a marked increase in collagen deposition, a critical factor in tissue regeneration and wound strength, thereby suggesting an expedited healing trajectory. Complementing these findings, real-time dynamic assessments using advanced ultrasound and photoacoustic imaging techniques provided compelling evidence of enhanced vascularity, improved oxygen saturation, and robust angiogenesis within the wound environment, all of which are essential parameters for successful wound repair. Despite these promising outcomes, the study's scope was limited to MDR bacterial strains isolated from local hospitals and focused exclusively on a single nanofiber-based drug delivery system. To fully realize the translational potential of this technology, future investigations should expand to include alternative delivery platforms and a broader spectrum of MDR pathogens from diverse geographic regions. In conclusion, the G-S-CMC-Pep-NPs-NFs dressing emerges as a promising and innovative framework for the development of next-generation antibacterial agents with significant wound healing capabilities, offering a potential solution to the pressing clinical challenge of MDR-infected wounds.